113
2-19-76

Dr-2042

LA-6019

UC-34c
Reporting Date: June 1975
Issued: January 1976

Negative Ion Beam Processes

by

T. D. Hayward
G. P. Lawrence
R. F. Bentley
J. J. Malanify
J. A. Jackson

los alamos
scientific laboratory
of the University of California
LOS ALAMOS, NEW MEXICO 87545

UNITED STATES
ENERGY RESEARCH AND DEVELOPMENT ADMINISTRATION
CONTRACT W-7405-ENG. 36

Printed in the United States of America. Available from
National Technical Information Service
U.S. Department of Commerce
5285 Port Royal Road
Springfield, VA 22161
Price: Printed Copy $6.00 Microfiche $2.25

CONTENTS

NEGATIVE ION BEAM PROCESSES

by

T. D. Hayward, G. P. Lawrence,
R. F. Bentley, J. J. Malanify,
and J. A. Jackson

ABSTRACT

Los Alamos Scientific Laboratory fiscal year 1975 work on production of intense, very bright, negative hydrogen (H^-), ion beams and conversion of a high-energy (a few hundred MeV) negative beam into a neutral beam are described. The ion source work has used a cesium charge exchange source that has produced H^- ion beams ≥10 mA (about a factor of 10 greater than those available 1 yr ago) with a brightness of 1.4×10^9 A/m^2-rad^2 (about 18 times brighter than before). The high-energy, neutral beam production investigations have included measurements of the 800-MeV H^--stripping cross section in hydrogen gas (σ_{-10}, tentatively 4×10^{-19} cm^2), 3- to 6-MeV H^--stripping cross sections in a hydrogen plasma (σ_{-10}, tentatively $2\text{-}4 \times 10^{-16}$ cm^2), and the small-angle scattering that results from stripping an 800-MeV H^- ion beam to a neutral (H^0) beam in hydrogen gas. These last measurements were interrupted by the Los Alamos Meson Physics Facility shutdown in December 1974, but should be completed early in fiscal year 1976 when the accelerator resumes operation. Small-angle scattering calculations have included hydrogen gas-stripping, plasma-stripping, and photodetachment. Calculations indicate that the root mean square angular spread of a 390-MeV negative triton (T^-) beam stripped in a plasma stripper may be as low as 0.7 μrad.

I. HIGH-ENERGY H^--STRIPPING FRACTIONS

When a high-energy H^- beam is passed through a "thin" target, charge-changing occurs because of collisions between beam and target. The processes and relevant cross sections are

$$H^- + x \rightarrow H^0 + e^- + x^* \quad , \sigma_{-10} \quad , \tag{1}$$

$$H^- + x \rightarrow H^+ + 2e^- + x^* \quad , \sigma_{-11} \quad , \tag{2}$$

$$H^0 + x \rightarrow H^+ + e^- + x^* \quad , \sigma_{01} \quad , \tag{3}$$

$$H^0 + x \rightarrow H^- + x^{+*} \quad , \sigma_{0-1} \quad , \tag{4}$$

$$H^+ + x \rightarrow H^0 + x^{+*} \quad , \sigma_{10} \quad , \tag{5}$$

$$H^+ + x \rightarrow H^- + x^{++*} \quad , \sigma_{1-1} \quad . \tag{6}$$

In these processes, x represents the target material, which may be atoms, molecules, ions, free electrons, or photons, and x* represents the target after the charge-changing collision, the * indicating that the target may be in an excited state that includes a free electron ion system.

Processes (4)-(6) are beam electron pickup reactions, and at beam energies above a few tens of keV they are dominated by the beam electron-stripping processes, (1)-(3). All the reactions may be important in H^- ion source beam formation, depending upon x and the beam energy. This discussion concerns the stripping processes at energies of a few tens to a few hundreds of millions of electron volts.

An H^- beam incident on a stripping target gives three charged beams, H^-, H^0, and H^+. The differential equations that govern growth and decay of these beams are

$$\frac{dN_-}{d\chi} = -(\sigma_{-10} + \sigma_{-11})N_- \quad , \tag{7}$$

$$\frac{dN_0}{d\chi} = \sigma_{-10} N_- - \sigma_{01} N_0 \quad , \tag{8}$$

$$\frac{dN_+}{d\chi} = \sigma_{-11} N_- + \sigma_{01} N_0 \quad , \tag{9}$$

where $\chi \equiv$ number of target atoms, ions, etc., per square centimeter in the stripping target, and N_-, N_0, and N_+ are the fractions of H^-, H_0, and H^+ in the beam. The solutions of Eqs. (7)-(9) are

$$N_- = \exp\left[-(\sigma_{-10} + \sigma_{-11})\chi\right] \quad , \tag{10}$$

$$N_0 = \frac{\sigma_{-10}}{\sigma_{-10} + \sigma_{-11} - \sigma_{01}} \left\{\exp(-\sigma_{01}\chi) - \exp\left[-(\sigma_{-10} + \sigma_{-11})\chi\right]\right\} \quad , \tag{11}$$

$$N_+ = 1 - \frac{1}{\sigma_{-10} + \sigma_{-11} - \sigma_{01}} \left\{\sigma_{-10} \exp(-\sigma_{01}\chi) - (\sigma_{01} - \sigma_{-11}) \exp\left[-(\sigma_{-10} + \sigma_{-11})\chi\right]\right\} . \tag{12}$$

The optimum target thickness χ_m that produces the largest H^0 beam is found by setting the derivative of N_0, Eq. (11), with respect to χ equal to zero.

$$\left.\frac{dN_0}{d\chi}\right|_{\chi = \chi_m} = 0 \quad . \tag{13}$$

This yields

$$\chi_m = \frac{1}{\sigma_{-10} + \sigma_{-11} - \sigma_{01}} \ln\left(\frac{\sigma_{-10} + \sigma_{-11}}{\sigma_{01}}\right) \quad . \tag{14}$$

Figure 1 indicates the amount of the beam in each charge state vs the normalized target thickness χ/χ_m for a hydrogen gas target. Because the stripping cross sections all scale with essentially the same beam energy dependence, Fig. 1 represents the process at all beam energies of interest and with a hydrogen gas target. It shows that the maximum amount of H^- beam converted to an H^0 beam is <0.6.

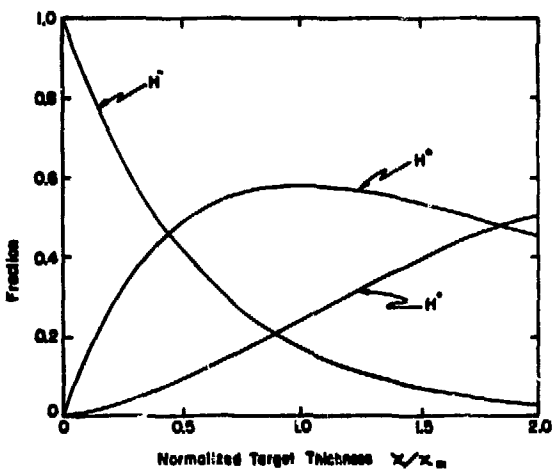

Fig. 1.
Amount of incident H^- beam in various charge states vs H_2 gas stripper thickness.

II. MINIMUM ANGULAR SPREAD INTRODUCED IN NEGATIVE ION BREAKUP (C. M. MOTION)

A Y^- complex ion can be considered classically as a Y^0 particle and an electron orbiting about the center of mass (c.m.) of the complex (Fig. 2). For a $1/r^2$ coulomb force, the virial theorem gives $-E_B = E_{kl}$, whereas, for a $1/r^7$ van der Waals-type force, the equivalent virial theorem gives $-E_B = 2E_{kl}/3$ ($E_{kl} \equiv$ internal kinetic energy and $E_B \equiv$ negative ion binding energy). These can be written as

$$-E_B = \frac{p_e^2}{2m_e} + \frac{p_{Y^0}^2}{2m_{Y^0}} \quad \text{coulomb,} \tag{15a}$$

and

$$-E_B = \frac{2}{3}\left(\frac{p_e^2}{2m_e} + \frac{p_{Y^0}^2}{2m_{Y^0}}\right) \quad \text{van der Waals.} \tag{15b}$$

These two types of forces are listed because they represent, to some extent, the extreme r dependence for the force that binds the Y^- system.

In the c.m., $\vec{P}_e = -\vec{P}_{Y^0}$ and, because $m_e \ll m_{Y^0}$, the leading terms in Eqs. (15) dominate and the Y^0 velocity is given by

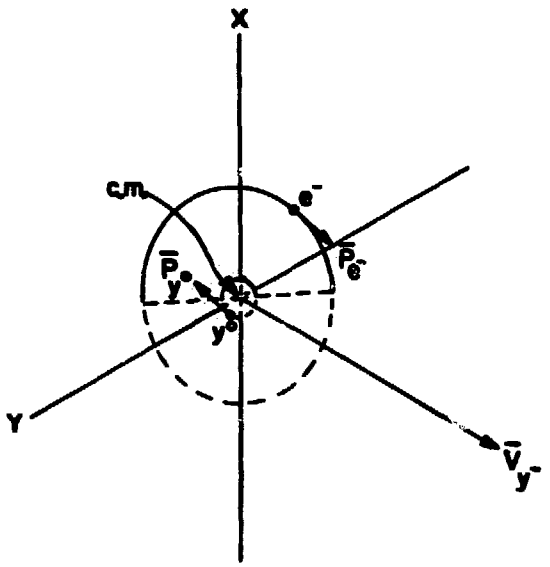

Fig. 2.
Y^0 motion about Y^- c.m. The projection of $\vec{P}_{Y^0}$ on the x-y plane averaged for all orientations of the Y^0 orbit determines the intrinsic angular spread $\langle\theta_I\rangle$ induced when the Y^- is stripped.

$$v_{Y^0} \approx \sqrt{-2m_eE_B/m_{Y^0}} \quad \text{coulomb,} \tag{16a}$$

and

$$v_{Y^0} \approx \sqrt{-3m_eE_B/m_{Y^0}} \quad \text{van der Waals.} \tag{16b}$$

In the sudden approximation, the Y^0 retains this motion with respect to the c.m., that is, relative to the original Y^- motion. To evaluate the angular spread introduced by this effect, one must average the projection of the induced motion on a plane perpendicular to the Y^- velocity V_{Y^-} (Fig. 2).

$$\langle\theta_I^2\rangle = \frac{\int_o^{\pi/2}\left(\frac{v_{Y^0}\sin\theta}{V_{Y^-}}\right)^2 2\pi\sin\theta d\theta}{\int_o^{\pi/2} 2\pi\sin\theta d\theta} \quad . \tag{17}$$

$$\langle\theta_I\rangle = \sqrt{\frac{2}{3}}\frac{v_{Y^0}}{V_{Y^-}} \quad . \tag{18}$$

Because the kinetic energy of the Y^- is

$$E_k = \frac{1}{2}m_{Y^-}(V_{Y^-})^2 \approx \frac{1}{2}m_{Y^0}(V_{Y^0})^2 \quad , \tag{19}$$

$$\langle\theta_I\rangle \approx 0.816\sqrt{\frac{-m_eE_B}{m_{Y^0}E_k}} \quad \text{coulomb,} \tag{20a}$$

and

$$\langle\theta_I\rangle = \sqrt{\frac{-m_eE_B}{m_{Y^0}E_k}} \quad \text{van der Waals.} \tag{20b}$$

The binding energy of negative hydrogen isotopes is H^-, D^-, and T^-, $-E_B$, = 0.75 eV. Choosing E_k = 250 MeV gives the results shown in Table I.

TABLE I

$\langle\theta\rangle$	coulomb	van der Waals
	= 1.04 μrad H^0	1.28 μrad H^0
	= 0.74 μrad D^0	0.91 μrad D^0
	= 0.60 μrad T^0	0.74 μrad T^0

Within the limits that the classical model presented here represents extremes of the internal motion of the negative ion system, these values give the intrinsic angular spread introduced in the stripping process, independent of its detailed nature.

Note that the ranges of H, D, and T ions in a given target material differ at a given energy. To keep the ion range the same as a 250-MeV H ion in aluminum, one must increase the energies of the D and T ions to approximately 290 and 390 MeV, respectively. For such a criterion, the following table can be constructed.

TABLE II

Ion	T(MeV)	$\langle\theta_1\rangle$ Coulomb (μrad)	$\langle\theta_1\rangle$ van der Waals (μrad)
H^+	250	1.04	1.28
D^+	290	0.69	0.84
T^+	390	0.48	0.59

III. CLASSICAL COULOMB SCATTERING DURING STRIPPING

The expected gas-stripping cross section of H^- at 250 MeV in hydrogen gas is about $\sigma_{-10} \sim 1\text{-}3 \times 10^{-19}$ cm^2. To convert a reasonable part of the H^- beam to an H^0 beam, $\sigma_{-10}\chi \sim 1$ (χ ≡ number of stripping gas atoms/cm^2). This implies a reasonable probability for collisions with impact parameters $\rho \sim 3 \times 10^{-10}$ cm. well within the hydrogen Bohr radius.

As a preliminary calculation of the angular spread introduced in the beam by these close collisions, we present a nonrelativistic classical coulomb scattering calculation. In the c.m. for small scattering angles, the coulomb scattering angle (ϕ_{cm}) is given by

$$\phi_{cm} = \frac{Z_1 Z_2 e^2}{4\pi\epsilon_0 (1/2\mu V^2)\rho} \quad \text{(mks units)} \quad , \tag{21}$$

where

Z_1 ≡ projectile atomic number ,
Z_2 ≡ target atomic number ,
e ≡ electron charge ,
ϵ_0 ≡ permeability of free space ,
ρ ≡ impact parameter ,
V ≡ velocity of the incident particle ,
μ ≡ reduced mass = $m_1 m_2/(m_1 + m_2)$.

The transformation between the c.m. and the laboratory angle θ is given by

$$\tan\theta = \frac{\sin\phi_{cm}}{\cos\phi_{cm} + m_1/m_2} \quad , \tag{22}$$

which for small angles becomes

$$\theta = \phi_{cm}\frac{m_2}{m_1 + m_2} \quad . \tag{23}$$

Thus, in the laboratory frame,

$$\theta = \frac{Z_1 Z_2 e^2}{4\pi\epsilon_0 (1/2m_1 V^2)\rho} = \frac{Z_1 Z_2 e^2}{4\pi\epsilon_0 E_k \rho} \quad , \tag{24}$$

where E_k is the kinetic energy of the incident particle. To simplify the equations, we define

$$D \equiv \frac{Z_1 Z_2 e^2}{4\pi\epsilon_0 E_k} \quad . \tag{25}$$

Then,

$$\theta = \frac{D}{\rho} \quad . \tag{26}$$

An rms scattering angle can be defined by averaging θ^2 (weighted by the differential cross section $d\sigma = 2\pi\rho d\rho$) over an appropriate range of impact parameters.

$$\langle\theta\rangle = \left(\frac{\int_{\rho_0}^{\rho_1} \theta^2\, 2\pi\rho d\rho}{\int_{\rho_0}^{\rho_1} 2\pi\rho d\rho}\right)^{1/2} \quad . \tag{27}$$

Here ρ_0 and ρ_1 are minimum and maximum values of ρ. Integration yields

$$\langle\theta\rangle = D\left(\frac{2\ln\frac{\rho_1}{\rho_0}}{\rho_1^2 - \rho_0^2}\right)^{1/2} \quad . \tag{28}$$

First consider the collision in which the H^- is converted to an H^0. For an impact parameter $\rho \leq \sqrt{(\sigma_{-11}/\pi)}$, the H^- is converted to an H^+. Thus, an effective minimum impact parameter is

$$\rho_0 = \left(\frac{\sigma_{-11}}{\pi}\right)^{1/2} \quad . \tag{29}$$

If ρ is too large, the H^- is not stripped and the collision is not of interest. So ρ must be less than ρ_1 given classically by

$$\pi\rho_1^2 - \pi\rho_2^2 = \sigma_{-10} \quad , \tag{30}$$

$$\rho_1 = \left(\frac{\sigma_{-10} + \sigma_{-11}}{\pi}\right)^{1/2} \quad . \tag{31}$$

One can thus define the rms angular spread introduced in the $H^- + x \rightarrow H^0 + x^+ + e^-$ stripping collision as

$$\langle \theta \rangle_{-10} = D \left[\frac{2\pi \ln\left(\frac{\sigma_{-10} + \sigma_{-11}}{\sigma_{-11}}\right)^{1/2}}{\sigma_{-10}}\right]^{1/2} \quad . \tag{32}$$

There are also collisions before the stripping collision in which the H^- is only scattered, not stripped. For those collisions,

$$\rho_0 = \sqrt{\frac{\sigma_{-10} + \sigma_{-11}}{\pi}} \quad , \tag{33}$$

and

$$\rho_2 = \rho_B = \sqrt{\frac{\sigma_B}{\pi}} \quad , \tag{34}$$

where ρ_B is the Bohr radius and σ_B is a Bohr cross section. For those collisions,

$$\langle \theta \rangle_{-1-1} = D \left[\frac{2\pi \ln\left(\frac{\sigma_B}{\sigma_{-10} + \sigma_{-11}}\right)^{1/2}}{\sigma_B - \sigma_{-10} - \sigma_{-11}}\right]^{1/2} \quad . \tag{35}$$

Finally, there are collisions after the stripping collision in which the H^0 is only scattered, not stripped to H^+. For those collisions,

$$\rho_0 = \sqrt{\frac{\sigma_{01}}{\pi}} \quad , \tag{36}$$

$$\rho_1 = \sqrt{\frac{\sigma_B}{\pi}} \quad , \tag{37}$$

and Eq. (27) yields

$$\langle \theta \rangle_{00} = D \left[\frac{2\pi \ln\left(\frac{\sigma_B}{\sigma_{01}}\right)^{1/2}}{\sigma_B - \sigma_{01}}\right]^{1/2} \quad . \tag{38}$$

The expected angular spread in the H^0 beam as a result of the collisions suffered in the charge exchange cell is the appropriate rms average of the intrinsic c.m. motion of the H^0 in the H^- system and the angles $\langle\theta\rangle_{-10}$, $\langle\theta\rangle_{-1-1}$, and $\langle\theta\rangle_{00}$.

After penetrating a distance χ into the target, the H^- beam fraction is

$$N_-(\chi) = \exp[-(\sigma_{-10} + \sigma_{-11})\chi] \quad . \tag{39}$$

The number of H^0's formed in the element between χ and $\chi + d\chi$ is

$$dN_0 = N_-(\chi)\sigma_{-10}d\chi \quad . \tag{40}$$

Of these neutrals, a fraction f survives to the end of the target (χ_0).

$$f(\chi) = \exp[-\sigma_{01}(\chi_0 - \chi)] \quad . \tag{41}$$

These H^0's suffer η_{-1-1} collisions as H^-'s with an rms angle $\langle\theta\rangle_{-1-1}$.

$$\eta_{-1-1}(\chi) = (\sigma_B - \sigma_{-10} - \sigma_{-11})\chi \quad . \tag{42}$$

They also suffer η_{00} collisions as H^0's with an rms angle $\langle\theta\rangle_{00}$.

$$\eta_{00}(\chi) = (\sigma_B - \sigma_{01})(\chi_0 - \chi) \quad . \tag{43}$$

The differential mean square angular deflection of the final H^0 beam that originated in the element $d\chi$ about χ as the result of nonstripping collisions weighted by the probability of formation and survival $[f(\chi)N_-(\chi)\sigma_{-10}\,d\chi]$ is

$$\langle \theta(\chi) \rangle^2_{-1-1,00} d\omega = [\eta_{-1-1}(\chi)\langle \theta \rangle^2_{-1-1} + \eta_{00}(\chi)\langle \theta \rangle^2_{00}] \cdot f(\chi)N_-(\chi)\sigma_{-10}d\chi \quad , \tag{44}$$

and mean square angular deflection is obtained by integration.

$$\langle \theta \rangle^2_{-1,-1,\infty} = \frac{\int_{\chi=0}^{\chi_0} \langle \theta(\chi) \rangle^2_{-1,-1,\infty} d\chi}{\int_{\chi=0}^{\chi_0} d\chi} \quad . \tag{45}$$

To simplify the resulting expression, we define

$$\sigma = \sigma_{-10} + \sigma_{-11} - \sigma_{01} \quad . \tag{46}$$

The integral then yields

$$\langle \theta \rangle^2_{-1,-1,\infty} = \frac{\sigma}{1 - \exp(-\sigma\chi_0)} \left[\frac{(\sigma_B - \sigma_{-10} - \sigma_{-11}) \langle \theta \rangle^2_{-1,-1} - (\sigma_B - \sigma_{01}) \langle \theta \rangle^2_{01}}{\sigma^2} \right] \cdot \left[1 - (\sigma\chi_0 + 1) \exp(-\sigma\chi_0) \right] + \left[\frac{(\sigma_B - \sigma_{01}) \langle \theta \rangle^2_{01} \chi_0}{\sigma} \right] \left[1 - \exp(-\sigma\chi_0) \right] \quad . \tag{47}$$

This expression is valid for either gas or plasma stripping using the relevant cross sections and by replacing σ_B with $\pi\rho_s^2$ where ρ_s is an appropriate plasma-screening radius. One added complication in plasma stripping is that collisions between the incident particle and both the plasma electrons and ions must be considered.

Finally, the total rms angular spread introduced in the H^0 beam by its formation in, and passage through, the stripping target is

$$\langle \theta \rangle = (\langle \theta_I \rangle^2 + \langle \theta \rangle^2_{10} + \langle \theta \rangle^2_{-1,-1,\infty})^{1/2} \quad . \tag{48}$$

Note that a shielded rms angular spread was calculated using ground state hydrogen wave functions and integrating the Coulomb scattering to ∞ rather than ρ_B. The resulting $\langle\theta\rangle$ changed by only 2% from the unshielded calculation which terminated at ρ_B.

IV. $\langle\theta\rangle$ HYDROGEN-GAS STRIPPING CALCULATIONS

Figures 3 and 4 show the experimental H^--stripping cross sections σ_{-10}, σ_{01}, and σ_{-11} in hydrogen as a function of H^- kinetic energy. The data below 20 MeV are from Refs. 1-5 and this plasma-stripping experiment. The datum at 800 MeV is from Los Alamos Meson Physics Facility (LAMPF) Experiment 128. The solid, smooth curves were obtained by scaling the cross sections with the H^+ energy loss rate $dE_k/d\chi$.[6] This scaling differs from the Born approximation predictions that the σ's should scale as $1/v^2$ (dashed curves).

The H^--stripping cross sections at 250 MeV were taken from the smooth curve $\sigma \propto dE_k/d\chi$;

$$\left.\begin{aligned} \sigma_{-10} &= 2.2 \times 10^{-19} \text{ cm}^2 \\ \sigma_{01} &= 5.8 \times 10^{-20} \text{ cm}^2 \\ \sigma_{-11} &= 7.5 \times 10^{-21} \text{ cm}^2 \end{aligned}\right\} \text{ per atom.} \tag{49}$$

Using these numbers to evaluate Eq. (32) gives $\langle\theta\rangle_{-10} = 4.0$ μrad. Taking the larger value of $\langle\theta_1\rangle$ from Table I (van der Waals) gives $\langle\theta_I\rangle = 0.91$ μrad. Equation (48) is evaluated with the aid of Eq. (47). Figure 5 plots $\langle\theta\rangle$ for a given χ against N_0, Eq. (11), for the same χ.

As $\chi \to 0$, $N_0 \to 0$, but $\langle\theta\rangle \to \sqrt{\langle\theta_1\rangle^2 + \langle\theta\rangle^2_{10}}$. That is, a very thin stripper converts a very small part of the H^- beam to H^0, but that which is converted is spread by the intrinsic c.m. motion and stripping-collision induced angular spreading. As the target thickens, N_0 increases to its maximum of 0.57 and then decreases while the angular spread continues to increase as a result of nonstripping collisions. At maximum N_0, $\langle\theta\rangle$ is 9.0 μrad.

Unfortunately, the entire curve lies to the right of the desired 1-μrad angular spread. It does, however, shift to the left when certain parameters are varied. To understand the behavior of the curve, one can examine the terms in Eq. (48) and their strongest parametric dependences. At maximum N_0, the terms are

$$\langle \theta_I \rangle = 1.28 \text{ μrad},$$

$$\langle \theta \rangle_{-10} = 4.0 \text{ μrad},$$

$$\langle \theta \rangle_{-1,-1,\infty} = 8.0 \text{ μrad}.$$

Equation (20) can be written as

$$\langle \theta_I \rangle = b \sqrt{\frac{m_e E_B}{m\gamma_0 E_k}} \quad . \tag{50}$$

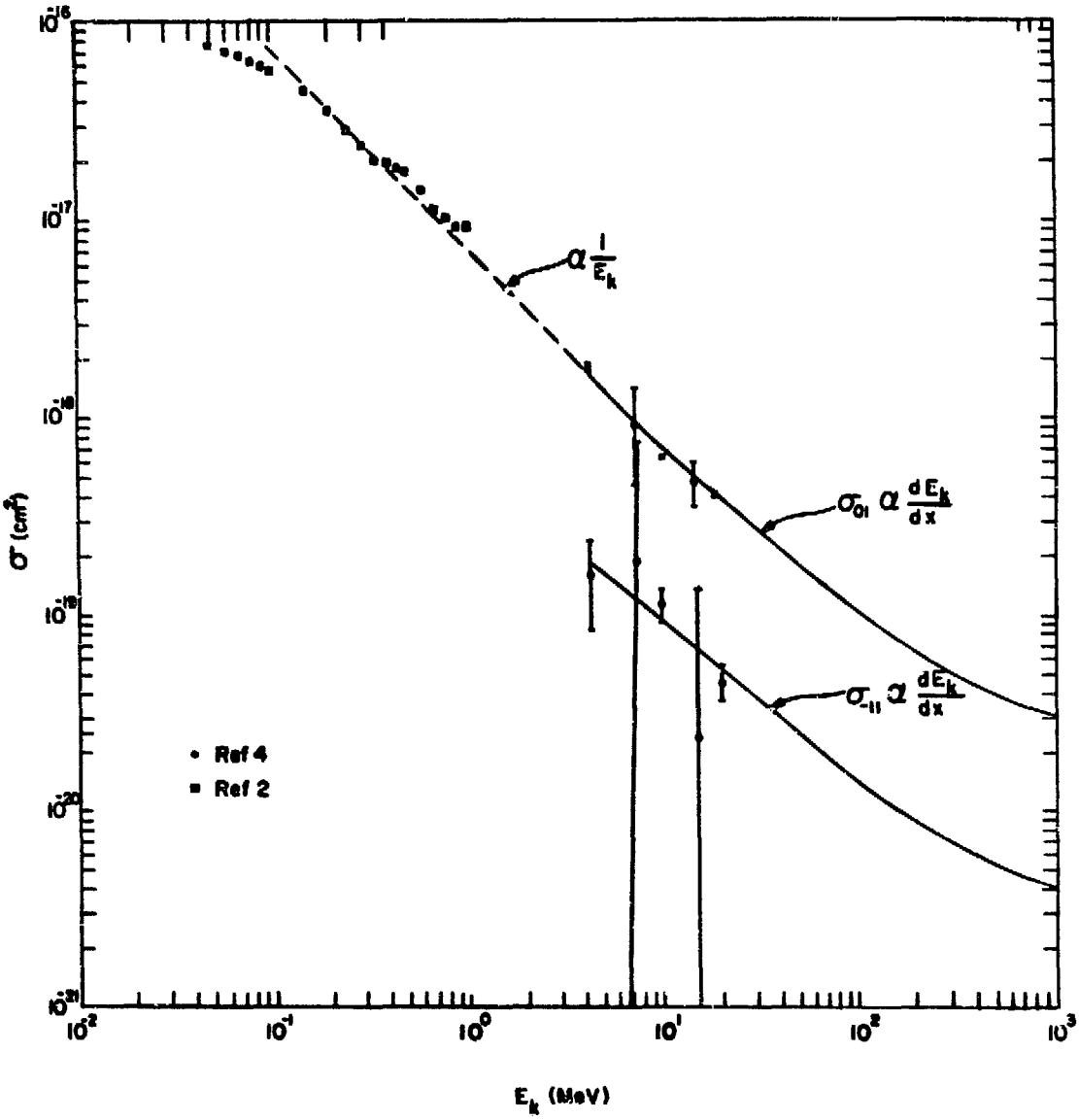

Fig. 3.
H^- -stripping cross sections σ_{01} and σ_{-11} in hydrogen gas vs H^- kinetic energy.

The constant b depends only on geometrical quantities and the form of the negative-ion binding potential, so it is fixed. Therefore, $\langle\theta_1\rangle$ can be decreased only by increasing the beam particle mass (m_{Y^0}) and/or kinetic energy E_k. Remember that increasing m_{Y^0} decreases the particle range in the target, so E_k must increase to maintain the same range. Clearly, increasing m_{Y^0} helps reduce $\langle\theta_1\rangle$.

It is also possible to reduce E_B and thus $\langle\theta_1\rangle$ by choosing a different ion type [$E_B(H^-) = 0.75$ eV, $E_B(He^-) = 0.07$ eV]. This approach is probably poor, because as $E_B \to 0$ the ion source brightness goes rapidly to zero.

Equation (32) can be expanded with the aid of Eq. (25) to give

$$\langle\theta\rangle_{-10} = \frac{Z_1 Z_2 e^2}{4\pi\epsilon_0 E_k}\left[\frac{2\pi \ln\left(\frac{\sigma_{-10}+\sigma_{-11}}{\sigma_{-11}}\right)^{1/2}}{\sigma_{-10}}\right]^{1/2}. \quad (51)$$

Increasing E_k reduces the angle, whereas increasing the ion mass has no effect except through

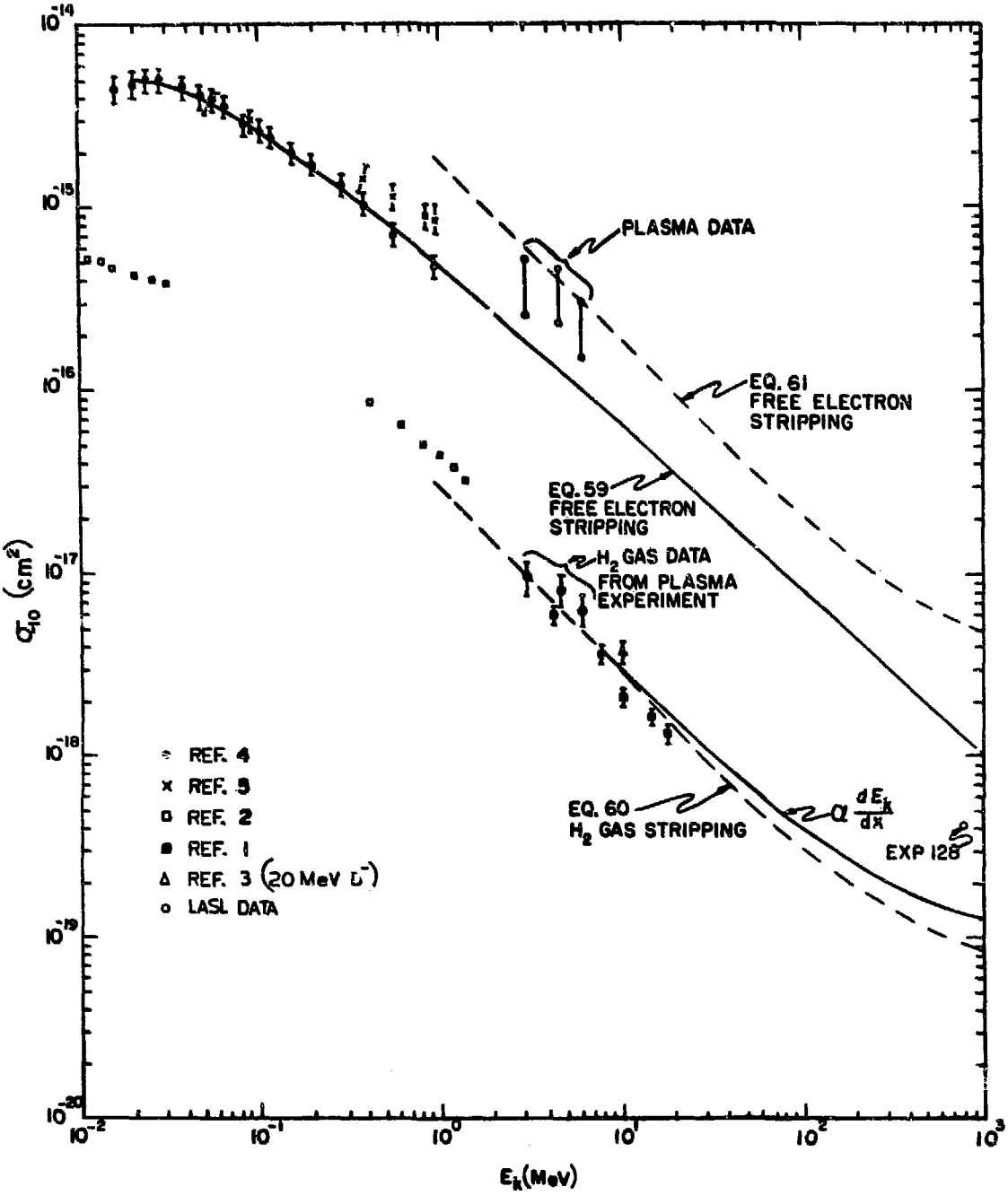

Fig. 4.
H^- -stripping cross section σ_{-10} in hydrogen gas and by free electrons vs H^- kinetic energy.

the required E_k increase and increased σ_{-10}. This last point requires explanation. In Ref. 3, 20-MeV D^--stripping cross sections were compared with 10-MeV H^--stripping cross sections. A 20-MeV D^- has the same velocity as a 10 MeV H^-. The comparison seems reasonable and agrees with the Born approximation prediction[7] that $\sigma \propto 1/v^2$.

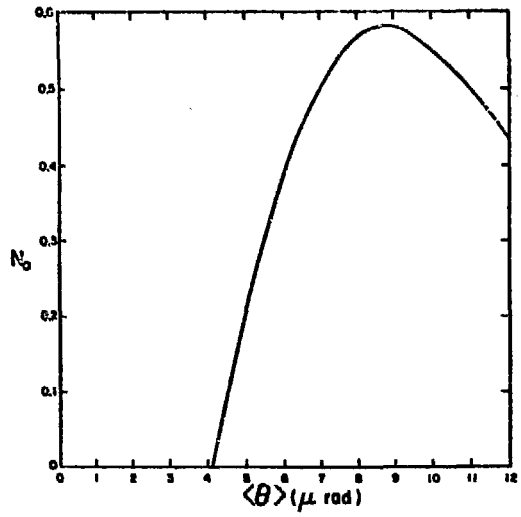

Fig. 5.
The fraction (N_0) of a 250-MeV H^- beam converted to an H^0 beam vs the calculated rms angular spread ($\langle\theta\rangle$) resulting from stripping in hydrogen gas.

This agreement implies that

$$\sigma_{-10}(D^-, 290\ \text{MeV}) = 2\,\frac{250}{290}\,\sigma_{-10}(H^-, 250\ \text{MeV}) ,$$

$$= 1.72\ \sigma_{-10}(H^-, 250\ \text{MeV}) ,$$

$$\sigma_{-10}(T^-, 390\ \text{MeV}) = 1.92\ \sigma_{-10}(H^-, 250\ \text{MeV}) . \quad (52)$$

Further increases in σ_{-10} can be obtained by stripping from free electrons, a hydrogen plasma, or photons. This stripping is discussed in more detail later.

The ln term in Eq. (51) is insensitive, and if the ratios of the various stripping cross sections are independent of the energy, as they seem to be, the ln term is a constant. The leading terms, Z_1 and Z_2, must clearly be kept as low as possible, implying the use of hydrogen isotopes. The final and dominating term $\langle\theta\rangle_{-1-1,00}$ is more complicated than those already discussed. For simplicity, the following stripping cross-section ratios will be assumed.

$$\sigma_{01} = 0.3\ \sigma_{-10} ,$$

$$\sigma_{-11} = 0.04\ \sigma_{-10} . \quad (53)$$

Equation (46) can now be written as

$$\sigma = 0.74\ \sigma_{-10} . \quad (54)$$

Further,

$$\sigma_B \gg \sigma_{-10}, \sigma_{01}, \sigma_{-11} . \quad (55)$$

When evaluated at $\chi_0 = \chi_m$ [Eq. (14)], the root of Eq. (47) then takes the form

$$\langle\theta\rangle^2_{-1-1,00})_m = \frac{1.05}{(N_0)_m}\sqrt{\frac{\sigma_B}{\sigma_{-10}}}\,(0.35\langle\theta\rangle^2_{-1-1} + 0.53\langle\theta\rangle^2_{00})^{1/2} , \quad (56)$$

where $(N_0)_m$ is the maximum value of N_0. Using Eqs. (25), (35), and (38) to expand, one gets

$$\langle\theta\rangle_{-1-1,00})_m = \frac{2.63}{(N_0)_m}\,\frac{Z_1Z_2e^2}{4\pi\epsilon_0 E_k}\sqrt{\frac{1}{\sigma_{-10}}}$$

$$\left[0.35\,\ln\left(\frac{\sigma_B}{\sigma_{-10}+\sigma_{-11}}\right)^{1/2} + 0.53\,\ln\left(\frac{\sigma_B}{\sigma_{01}}\right)^{1/2}\right]^{1/2} . \quad (57)$$

If the ln terms are ignored, the dependence is exactly the same as that for $\langle\theta\rangle_{-10}$, Eq. (51). The parametric dependence of Eqs. (50), (51), and (57) indicates that $\langle\theta\rangle$ will be reduced by increasing mv^0, E_k, and σ_{-10} while keeping $Z_1 = Z_2 = 1$.

Defining $\langle\theta\rangle_m$ as the angular spread in the beam with $\chi = \chi_m$ and choosing E_k for the different beam isotopes to give a fixed target material range, one gets for a hydrogen-gas stripping target

$$E_k = 250\ \text{MeV}, \langle\theta\rangle_m\ (H^-) = 9.0\ \mu\text{rad},$$
$$E_k = 290\ \text{MeV}, \langle\theta\rangle_m\ (D^-) = 5.9\ \mu\text{rad},$$
$$E_k = 390\ \text{MeV}, \langle\theta\rangle_m\ (T^-) = 4.1\ \mu\text{rad}. \quad (58)$$

Here, σ_{-10} for D^- and T^- was scaled using Eq. (52). Brueckner's independent Born approximation calculation[7] of $\langle\theta\rangle$ for H^- in a hydrogen gas stripper produced essentially the same results as the above coulomb calculation.

V. $\langle\theta\rangle$ PLASMA CALCULATIONS

In the previous section, we pointed out that changing the stripping medium so as to increase σ_{-10} reduces two of the three terms that contribute to

$\langle\theta\rangle_m$. One way to get such a result is to use the free electron H^--stripping process $H^- + e^- \rightarrow H^0 + 2e^-$.

Dance, Harrison, and Rundel[4] measured σ_{-10} for free electrons with crossed H^- and electron beams. Their measurements (electron energy = 505.6 eV) corresponding to an H^- energy of 0.929 MeV give $\sigma_{-10} = 4.7 \times 10^{-16}$ cm^2. The corresponding hydrogen-gas stripping cross-section measurements imply that $\sigma_{-10} \sim 2.7 \times 10^{-17}$ cm^2, indicating that the free-electron stripping cross section is about 17 times larger than the hydrogen-gas stripping cross section.

Dance et al.[4] give an analytic expression for the free-electron stripping cross section which can be written in terms of the H^- energy as

$$\sigma_{-10}(H^- + e^-) = \left(1 - \frac{6.86 \times 10^{-2}}{\sqrt{E_k \log_{10} 544 E_k}}\right)^{1.75} \frac{}{E_k} \cdot \log_{10} 591 E_k \times 10^{-16} \text{ cm}^2 , \quad (59)$$

where E_k is in million electron volts. This expression is plotted in Fig. 4 along with the data of Dance et al.[4] and Tisone and Branscomb,[5] transformed from electron energy to H^- energy. The expression should be valid for $E_k \gtrsim 20$ keV.

Brueckner[7] has derived Born approximation expressions for the total stripping cross section in free electron and hydrogen-gas stripping; he gets

hydrogen gas $$\sigma = 15.6\pi\left(\frac{V_0}{V}\right)^2 a_0^2 , \quad (60)$$

and

free electron $$\sigma = 960\pi\left(\frac{V_0}{V}\right)^2 a_0^2 , \quad (61)$$

where

$$V_0 = \frac{e^2}{\hbar} = 2.17 \times 10^8 \text{ cm/s} ,$$

$$V = p/m , \quad (62)$$

and

$$a_0 = 5.3 \times 10^{-9} \text{ cm} \quad \text{Bohr radius.} \quad (63)$$

The hydrogen-gas stripping expression, Eq. (60), agrees well with the experimental data up to about 20 MeV (see Fig. 4). At 800 MeV, it predicts $\sigma = 1 \times 10^{-19}$. The cross section measured in LAMPF Experiment 128 is tentatively assigned a value of 3.7×10^{-19} cm^2.

The free-electron stripping σ from Eq. (61) at 1 MeV is 2.1×10^{-15} cm^2, but σ_{-10} from Eq. (59) is 4.7×10^{-16} cm^2, about 4.5 times smaller. Because Eq. (59) correctly fits the free-electron stripping data below 1 MeV, it is used in later calculations. [At present, the plasma-stripping measurements set an upper bound consistent with Eq. (61).] Unfortunately, there are no experimental cross sections for σ_{-11} or σ_{01} in free electron stripping.

In these calculations, the ratios, Eq. (53), used for hydrogen gas stripping are assumed to apply to free electron stripping. We also assume that the cross sections for D^- and T^- scale according to Eq. (52). Actually, the free electrons would have to be confined in a plasma. Equation (57) $(\langle\theta\rangle_{-1-1,00})_m$ contains a screening cross section σ_B which, for the plasma, is assumed to be 10^{-10} cm^2, corresponding to a plasma density of about 10^{15} ions/cm^3. These assumptions were used to construct Table III which gives the neutral beam angular spread components for free electron stripping of H^-, D^-, and T^- with $\chi = \chi_m$. These results, particularly for T^-, are considerably more encouraging than the previous calculations for H^- in a hydrogen gas stripper.

VI. PHOTODETACHMENT

When the stripping target is composed of photons, the stripping fraction can approach 1.0 if the photon energy E_γ in the H^- rest frame lies between E_{BH^0} and E_{BH^-} where E_{BH^-} is the 0.75-eV H^- binding energy and E_{BH^0} is the 13.6-eV H^0 binding energy. Then, σ_{-10} is finite but $\sigma_{01} = 0$ and $\sigma_{-11} = 0$ if the two-step process $H^0 + \gamma \rightarrow H^{0*}$ and $H^{0*} + \gamma \rightarrow H^+ + e^-$ does not occur. It will not occur if the photon energy in the H^0 rest frame is less than the 10.2-eV H^{0*} first excited state. Figure 6 shows the photodetachment cross section $\sigma_{-10}(\gamma)$ as a function of the photon energy in the H^- rest frame.[8]

If σ_{-11} and σ_{01} are set equal to zero in Eq. (11), we have the expression for photodetachment.

$$N_0 = 1 - \exp(-\sigma_{-10}\chi) . \quad (64)$$

For $N_0 = 0.9$ and using the peak photodetachment cross section ($\sigma_{-10} = 4 \times 10^{-17}$ cm^2 at $E_\gamma = 1.46$ eV $= 2.3 \times 10^{-19}$ J), Eq. (64) implies a photon target thickness $\chi_\gamma = 5.75 \times 10^{16}$ photons/cm^2.

TABLE III

T (MeV)	Beam Ion	$\langle\theta_t\rangle$ (μrad)	$\langle\theta\rangle_{-10}$ (μrad)	$\langle\theta\rangle_{-1-1,00)m}$ (μrad)	$\langle\theta\rangle_m$ (μrad)	$\langle\theta\rangle_m$[a] (μrad)
250	H^-	1.28	0.97	2.2	2.7	1.7
290	D^-	0.84	0.61	1.5	1.8	1.2
390	T^-	0.59	0.45	1.0	1.2	0.8

[a] These values use the cross sections predicted by Eq. (61).

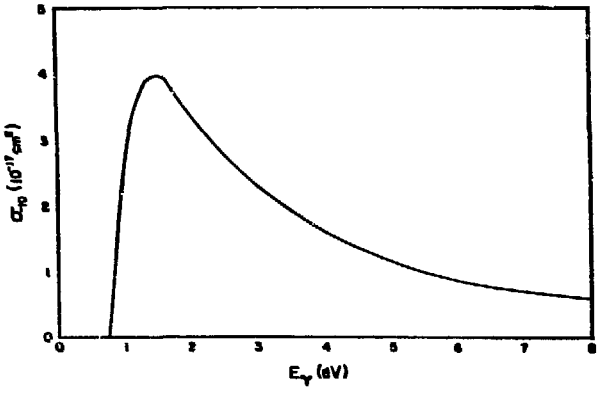

Fig. 6.
H^- photodetachment cross section (σ_{-10}) vs photon energy in the H^- rest frame.

A photodetachment cell can be thought of as two plane mirrors on opposite sides of the H^- beam (Fig. 7). A beam of light (possibly a laser) is directed across the ion beam, making a small angle with the normal to the mirror surface. If the mirror reflectivity is R, the photon density the beam sees is

$$\chi = \chi_0 + \chi_0 R + \chi_0 R^2 + \cdots + \chi_0 R^n = \chi_0 \sum_{i=0}^{n} R^i \quad , \qquad (65)$$

where χ_0 is the photon target density during the light's first passage across the cell and n is the number of reflections. Because $R \approx 1$ for a good mirror, the sum can be considered to be the Rieman Sum with $\Delta i = 1$,

$$\chi_0 \sum_{i=0}^{n} R^i \Delta i \rightarrow \chi_0 \int_{i=0}^{n} R^i di = \frac{\chi_0}{\ln R} (R^n - 1) \quad , \qquad (66)$$

for large n. Expressing R in the form

$$R = 1 - \delta, \ \delta << 1 \qquad (67)$$

reduces Eq. (66) to

$$\chi = \frac{\chi_0}{\delta} \quad . \qquad (68)$$

χ_0 is given in terms of the laser beam power P_L by

$$\chi_0 = \frac{P_L}{E_\gamma} \frac{1}{wc} \quad , \qquad (69)$$

where c is the speed of light and w is the width of the mirror system. Setting $\chi = \chi_\gamma$ in Eq. (68) and substituting from Eq. (69) for χ_0, we find P_L to be

$$P_L = \chi_\gamma E_\gamma wc\delta \quad . \qquad (70)$$

Assuming a good coated mirror R = 0.999 ($\delta = 10^{-3}$),

$$P_L = 40\ w\ (MW) \quad ,$$

where w is in meters. Given a laser efficiency $\epsilon_L = 0.1$ and a beam duty factor $\phi_B = 0.1$, the average power supply load $\bar{P}$ is

$$\bar{P} = P_L \frac{\phi_B}{\epsilon_L} = 40\ w\ (MW) \quad . \qquad (71)$$

Note that the only advantages of laser light over other light are that its low angular spread allows the mirror system to be used efficiently and its monochromaticity allows the mirror coating to be chosen so that δ is very small. Note also that the

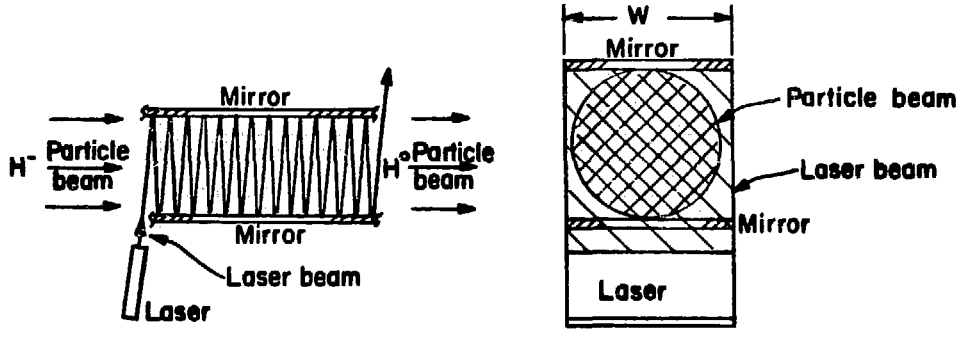

Fig. 7.
Photodetachment cell schematic.

preceding calculation did not take into account scattering of laser light out of the cell through interaction with the particle beam, or the relativistic Doppler shift of the photon energy. In any event, 40 MW/m of laser power is certainly excessive.

Equation (71) indicates that reducing the beam duty factor reduces the required laser power. This reduction, of course, reduces the particle beam average power unless the particle beam current is increased correspondingly, thus transferring part of the problem back to the accelerator and ion source.

VII. HYDROGEN-GAS STRIPPING MEASUREMENTS AT 800 MeV

LAMPF Experiment 128 was proposed in August 1972 to obtain experimental H^- stripping cross sections for a number of stripping materials of interest to the proposed 800-MeV Weapons Neutron Research (WNR) facility storage ring.[9] The experiment was run using Los Alamos Scientific Laboratory (LASL) funds in late 1974. Some results are reported here because they are the only high-energy (800-MeV) stripping data available.

The experiment is diagrammed in Fig. 8. In the H_2 gas-stripping part of the measurement, the 800-MeV LAMPF H^- beam was passed through a windowless, differentially pumped, 80-cm-long H_2 gas target, 1 cm high by 0.5 cm wide. The resulting H^-, H^0, and H^+ beams were then separated vertically in a 2° charge analysis magnet, passed through a thin (1.5-mm) aluminum vacuum window, and drifted 5.8 m through air to three scintillation detectors that single-particle counted the three beams. Immediately upstream from the detectors, the beams passed through three 7.6-cm-diam openings in a 1.8-m-thick magnetite concrete shield that effectively reduced the beam line background radiation.

The efficiencies of the detectors were corrected for by mechanically interchanging the top and middle detectors. The top and bottom detectors were then "effectively interchanged" by reversing the field in the charge analysis magnet.

The gas target density was determined by measuring the gas pressure profiles in the target with a calibrated McCloud gauge. One further sophistication was used for these measurements. A pure H^0 beam was produced by field stripping the H^- beam in an ~1.7-cm-long, (17-kG) magnetic field. This H^0 beam was then passed through the gas target to measure σ_{01} directly.

The H_2 -gas stripping measurement at 800 MeV tentatively yields

$$\sigma_{-10} = 3.7 \times 10^{-19} \text{ cm}^2/\text{atom} \qquad (72)$$

for σ_{-10} . This point is plotted in Fig. 4 with no error assignment, as data analysis is not yet complete. A more detailed description of the experiment and results for carbon, aluminum, and gold strippers is to be published.

VIII. <θ>SMALL-ANGLE SCATTERING EXPERIMENT

LAMPF Experiment 192 is designed to verify the small-angle scattering calculations developed in

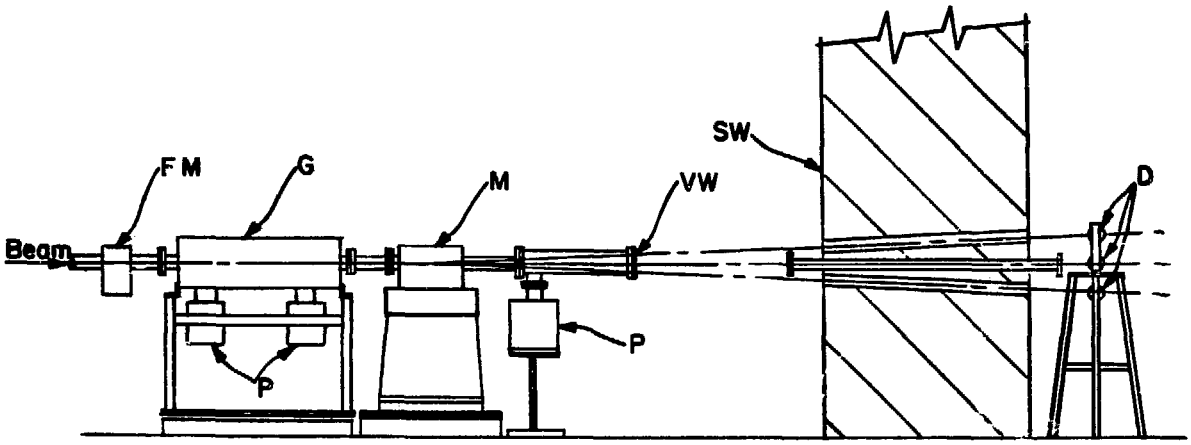

Fig. 8.
LAMPF Experiment 128, an 800-MeV H^- -stripping cross-section experiment. FM, field-stripping magnet; G, gas target chamber; P, ion pumps; M, charge analysis magnet; VW, aluminum vacuum window; SW, shield wall; D, beam detectors.

preceding sections of this report.[10] The measurements will be for 800-MeV H^- stripping in H_2 gas. To date, there seem to be no such experimental data at any energy.

Because the angular spread expected in the stripper gas at 800 MeV is a few microradians (see Fig. 9), it is necessary to produce a supercollimated H^- beam with an angular spread of about 1 μrad. This supercollimated beam is passed through a windowless gas target, and the resulting increase in angular spread is recorded as an increased supercollimator slit image on a photographic plate. Expected H^0 slit image widths are shown at the top of Fig. 9 for the experiment as described below.

Figure 10 shows the experimental arrangement in vertical and horizontal sections. Starting at the upstream end of the apparatus, the first element is a mechanical beam chopper (C_1). Its function is to pass a single LAMPF H^- macropulse per measurement. (A LAMPF macropulse is 500 μs long, and successive macropulses are separated by 8.33 ms.) The plan is to take a single measurement of the angular spread with a 500-μs beam pulse and thus reduce the angular spread introduced by mechanical vibrations and magnetic field changes within the apparatus.

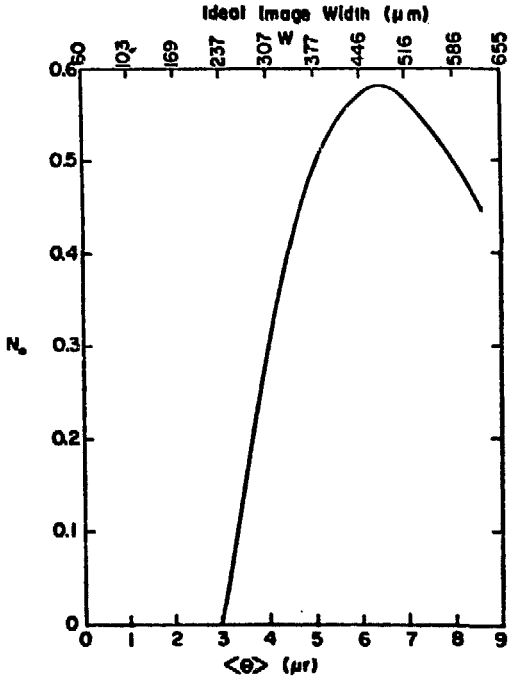

Fig. 9.
The fraction, N_0, of an 800-MeV H^- beam converted to an H^0 beam vs the calculated rms angular spread, <θ>, resulting from stripping in hydrogen gas. The scale at the top gives the slit image width expected in LAMPF Experiment 192, with the quadrupole lens turned off.

The beam chopper (Fig. 11) consists of two 15.24-cm-diam by 6.25-μm-thick aluminum disks. In the edge of each is a radial slot 1.9 cm long by 0.8 cm wide. The disks are driven by a synchronous motor with a 10:1 gear box which is located between them. One disk rotates at 600 rpm while the other rotates at 60 rpm. The slots overlap on the beam axis once each second and are open for 8 ms thus passing one H^- macropulse per second. Beam pulses arriving at times when the slots do not overlap are stripped to H^+ and rejected by the charge analysis magnet B_1.

The LAMPF beam is phase-locked to the 60-Hz utility power, and the chopper is phased with the beam by mechanically rotating the stator of the synchronous motor using a small stepping motor. To obtain single macropulses, a 5-cm by 5-cm by 6.25-μm-thick aluminum foil is positioned on the beam axis (closed position). The foil can be removed from the beam axis (open position) in 0.5 s by a stepping motor. It can also be "closed" in 0.5 s. The foil-actuating stepping motor is controlled by a fast relay logic circuit that uses a light and photocell to detect the chopping disks' positions about 0.25 s after they open on the beam axis. To obtain a single beam pulse, a toggle switch on the logic circuit is positioned to "set;" this initializes the logic. (The foil is in the closed position.) The toggle switch is then moved from set to "fire," and the next photocell pulse starts the logic sequence. The foil opens, the disks open and close, 0.25 s later the photocell sends a second pulse to the logic circuit, and the foil closes and remains closed until the set and fire sequence is repeated. Figure 12 shows this automatic time sequence. For beam tuning, the automatic time sequence can be disabled and the foil can be opened or closed by a manual switch. In the open position, tuning proceeds with one beam pulse per second.

Down the beam line and immediately adjacent to the chopper, is the first supercollimation slit, a 25-μm-high by 5-mm-wide opening in a 6-μm-thick nickel foil. Only the beam passing through the opening survives as H^-; that which strikes the foil is stripped to H^+ and discarded by the charge analysis magnet B_1. The H^- beam then drifts 50 m to a magnetic quadrupole doublet lens (L_1,L_2), used to form an image of S_1 on the photographic detection plate.

Immediately downstream from the lens is the second supercollimation slit S_2 (25 μm high by 5 mm wide in 6-μm nickel foil). At the second slit, H^-

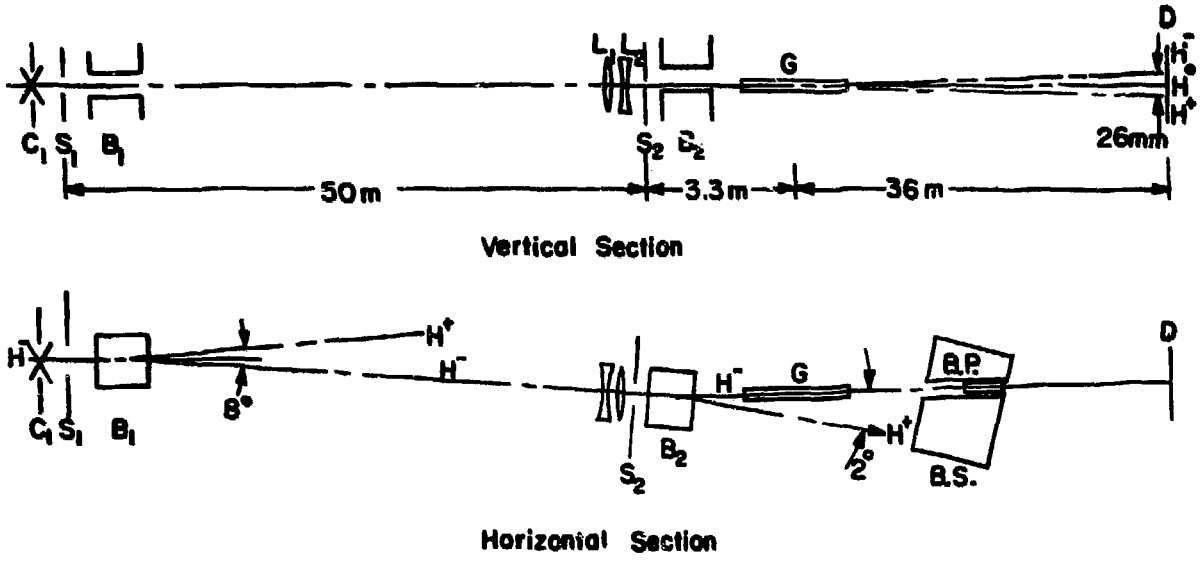

Fig. 10.
LAMPF Experiment 192. C_1, mechanical H^- beam chopper; S_1, first supercollimation slit; B_1, 4° charge analysis magnet; L_1, first element of magnetic quadrupole doublet lens; L_2, second element; S_2, second supercollimation slit; B_2, 1° charge analysis magnet; G, gas-stripping target; and D, photographic detector.

beam emittance has spread the beam to an 8-mm-wide by 3-mm-high spot. The beam spot must cover the slit but need not be accurately centered on it. Again, only the part of the beam which passes through the slit opening remains negative. Charge analysis magnet B_2 disposes of the stripped H^+ beam and bends the supercollimated H^- beam into the gas-stripping target.

Figure 13 shows the gas target, 86.4 cm long and 0.48 cm in diameter. It can operate at pressures of up to 10 torr and is differentially pumped in three stages. The first stage is pumped to 2×10^{-2} torr by an 800-cfm Roots-type blower package, the second stage is pumped to 5×10^{-5} torr by two diffusion pumps (one 2000-ℓ/s, the other 1000-ℓ/s). The third

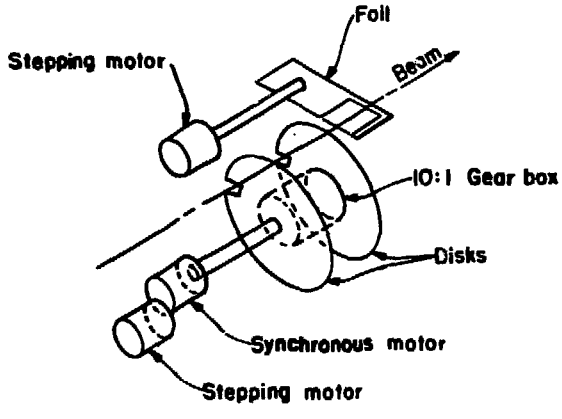

Fig. 11.
LAMPF Experiment 192 mechanical beam chopper.

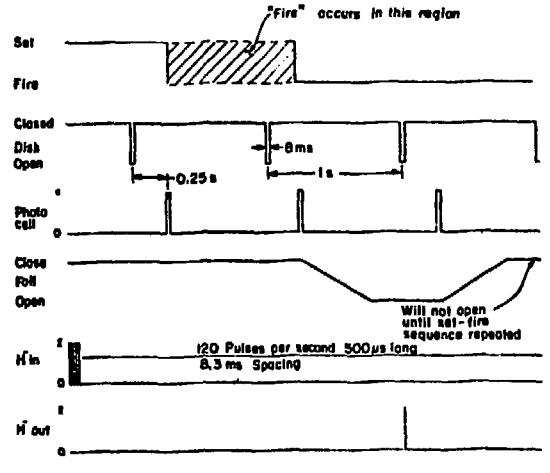

Fig. 12.
The time sequence of the mechanical beam chopper and the LAMPF beam.

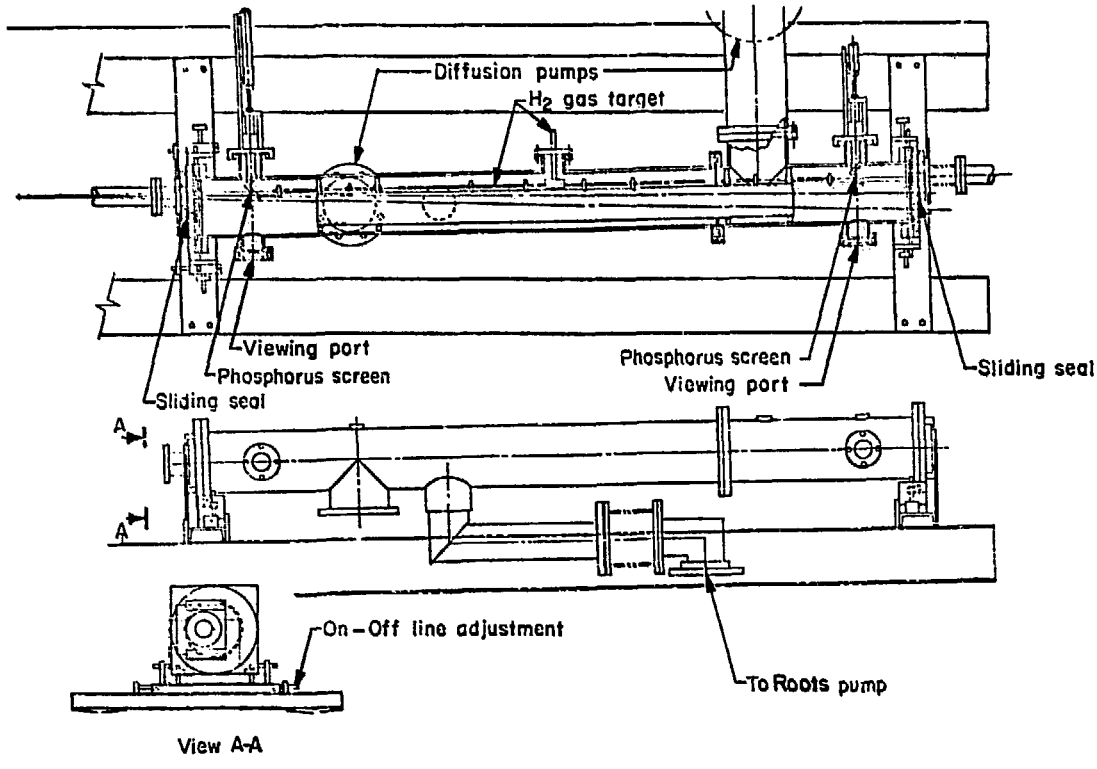

Fig. 13.
The gas target used in LAMPF Experiment 192.

stage is pumped by the beam line 600-ℓ/s ion pumps, one upstream from the target and two downstream.

In the gas target, depending upon its pressure, various fractions of the H^- beam are converted to H^0 and H^+. All three beams then drift through a beam stop to the photographic detection plate D. During the drift, the three beams (H^-, H^0, H^+) are separated vertically by earth's magnetic field to produce three images of S_1 on the photographic plate.

Current levels and particle numbers expected at various points along the experiment are listed in Table IV.

From the beam stop to the photographic plate, the beam line is unshielded; therefore the experiment can be run only during nights and weekends when personnel can be excluded from this area. To facilitate use of the beam line during the normal working day by other experiments set up along its length, it is necessary to insert a beam plug into the beam line where it penetrates the beam stop. This plug prevents the beam and its associated radiation from reaching the unshielded part of the beam line when other experiments are running.

Experiment 192 was first attempted in December 1974 just before the so-called LAMPF "Great Shutdown." Various operational problems including mechanical alignment between slit S_2 and the gas target and a bow introduced in the beam line when the beam stop (a 2000-ton, ~7.6-m^3 concrete and steel block) was restacked around the beam line, prevented data acquisition.

The accelerator is scheduled to restart operation for experiments about mid-September 1975. Experiment 192 has been scheduled tentatively for the first experimental run cycle. A number of apparatus modifications and improvements are being implemented, as follows.

A. Chopper

A rebuilt chopper (C_1) is 90% complete. The new design incorporates a 600-rpm stabilized hysteresis synchronous motor. The old design used a 60-rpm synchronous motor that had phase stability problems. Use of a 600-rpm motor allows the 10:1 gear box that couples the chopper disks to be driven

TABLE IV

	I_-	Macropulse $\langle I \rangle_-$	Macropulse N_-	N_0	N^+
Entering Chopper	1. μA	17. μA	5.3×10^{10}	---	---
Leaving Chopper (1 pulse/s)	8.3 nA	17. μA	5.3×10^{10}	---	---
Leaving S_1	3.3 pA	6.8 nA	2.1×10^{7}	---	---
Leaving S_2 Entering G	6.2×10^{-16} A	1.2 pA	$4. \times 10^{3}$	---	---
Detector Max N_0	---	---	$7. \times 10^{2}$	2.4×10^{3}	9×10^{2}

from the high-speed end and thus greatly reduces the lash induced in the phase stability between the disks. The phase instability in the previous design was acceptable, but extremely annoying.

The chopping mechanism has been made remotely removable from the beam line. Previously, this required "turning off" another experimental area and manually locking the chopping disk open, a process that proved unreliable.

B. Slit S_2

During the December experiment, S_2 was located ahead of the lens (L_1, L_2) about 2.3 m upstream from the gas target entrance. It is being moved downstream from the lens about 0.9 m from the gas target entrance. Also, it is mounted on a remote actuator so that it can be remotely positioned vertically. This should facilitate alignment between the slit and the gas cell. The new equipment is about 90% fabricated and tested.

C. Gas Target

The original gas target was a rectangular tube 2 mm high by 10 mm wide. It has been changed to a 4.8-mm-diam circular tube, further reducing the alignment problem. Also, the target can be aligned with the beam without breaking vacuum and phosphors can be placed at either end of the cell so that the beam can be observed during target alignment.

Normally the beam at this point is too weak to be observed on a phosphor by a standard T.V. system, we have bought and tested two intensified T.V. cameras. The new gas target is about 90% complete.

D. Beam Plug

During the December experiment, the beam plug was crude. It consisted of removing a section of beam line downstream from the beam stop, sliding a 1.2-m-long steel cylinder inside the beam line where it passed through the beam stop, blocking off the beam line, and placing a 3.5-ton concrete block over the end of it.

A new beam plug is 90% fabricated. It consists of five 60-cm-long cylinders. Two are each composed of a 30-cm-long steel-cased magnetite concrete cylinder and a 30-cm-long steel cylinder. The remaining three are 60-cm-long steel cylinders. The entire plug is housed (off the beam axis) in an oversized section of beam pipe downstream from the beam stop. The plug can be positioned on the beam axis and moved into the beam line inside the beam stop without breaking vacuum.

E. Detector

A film changer being planned will permit several measurements before requiring that the beam be turned off and the film be manually retrieved. Previously, only a single film could be exposed before retrieval. The conceptual design is complete, and mechanical drawings will be prepared.

IX. PLASMA-STRIPPING EXPERIMENT

This experiment is designed to extend the free electron stripping cross-section measurements for σ_{-10} to higher H^- energies and to develop the techniques for doing so with a plasma-stripping target rather than an electron beam. Further such measurements could indicate the plasma protons' role in the stripping process; i.e., whether as much stripping occurs from the protons as from the plasma electrons. The H^- energy range investigated was 3 to 6 MeV, chosen for the following reasons.

- H^- beams in this energy range are readily available from the LASL Group P-9 vertical Van de Graaff accelerator.
- The energy range is modestly above that of the existing experimental data.[4,5]
- Radiation levels at the lowest energy are low enough that personnel access to the plasma target can be maintained during data collection.

A. Experimental Apparatus

Figure 14 shows the experimental arrangement. The beam enters the plasma target by traveling down a hole bored axially through the poles of the magnet that provides the field for the Penning ion gauge (PIG) plasma discharge. After passing through the plasma and magnet, the beam is charge analyzed in a 1° bending magnet into H^-, H^0, and H^+ beams. These beams drift 2 m and are stripped to H^+ in 6-μm-thick aluminum foils. The H^+ beams are then collected in three Faraday cups and integrated by three charge digitizer and scaler systems. Stripped electrons and knock-on electrons from the stripping foils are kept from reaching the cups by a weak magnetic field produced by two permanent magnets.

Figure 15 shows the plasma target. There are two vacuum chambers. The outer is a 10-cm-diam stainless steel tube pumped directly by an unbaffled 1000-ℓ/s diffusion pump. The inner is an 8.9-cm-diam copper cylinder sealed at its lower end by a copper disk and box structure. The box has internal dimensions of 3.1 by 3.1 by 5 cm. Its top is open to the inner vacuum chamber. At each end of the box are 2.2-cm-diam openings each covered with a 0.8-mm-thick tantalum disk through the center of which a 2-mm-diam hole is bored. The beam enters and leaves the plasma cell through these holes, and the plasma discharge strikes between the tantalum disks (PIG cathodes) covering the holes. This inner vacuum chamber is pumped only through the beam entrance and exit holes. The filament leads, anode, plasma probe, and hydrogen gas supply enter the inner vacuum chamber through the chamber cover. The chamber cover is also fitted with a small glass port through which the plasma and its probe can be seen.

The pressure in the outer vacuum chamber was measured with an ion gauge, and the corresponding pressure in the inner chamber was determined accurately with a calibrated McCloud gauge. Also, provisions were made to inject the hydrogen into the outer chamber. This allowed us to verify that gas from the plasma cell produces a negligible H^0 background outside the cell.

Although determining hydrogen-gas stripping cross sections was not the original purpose of the experiment, these data were acquired in the normal

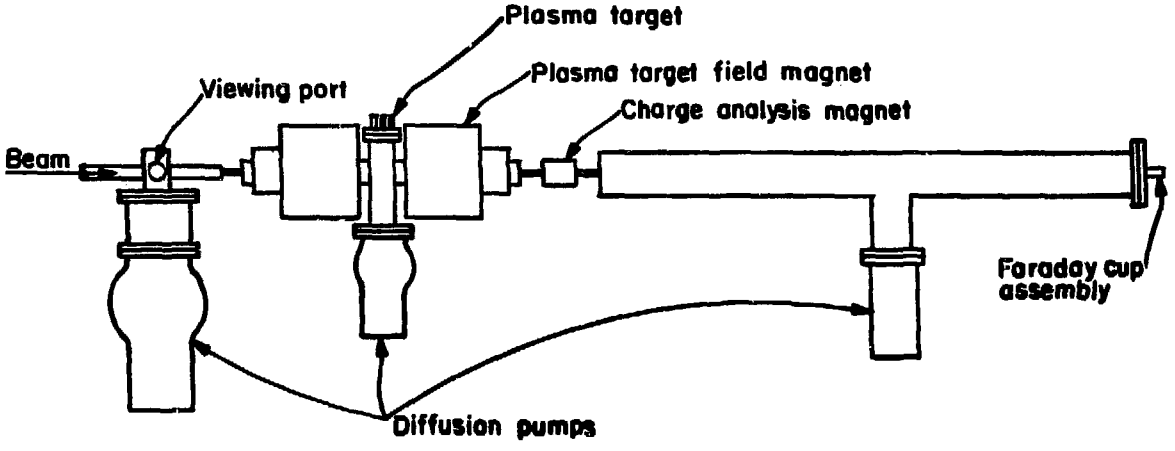

Fig. 14.
The H^- -plasma stripping cross-section experimental arrangement.

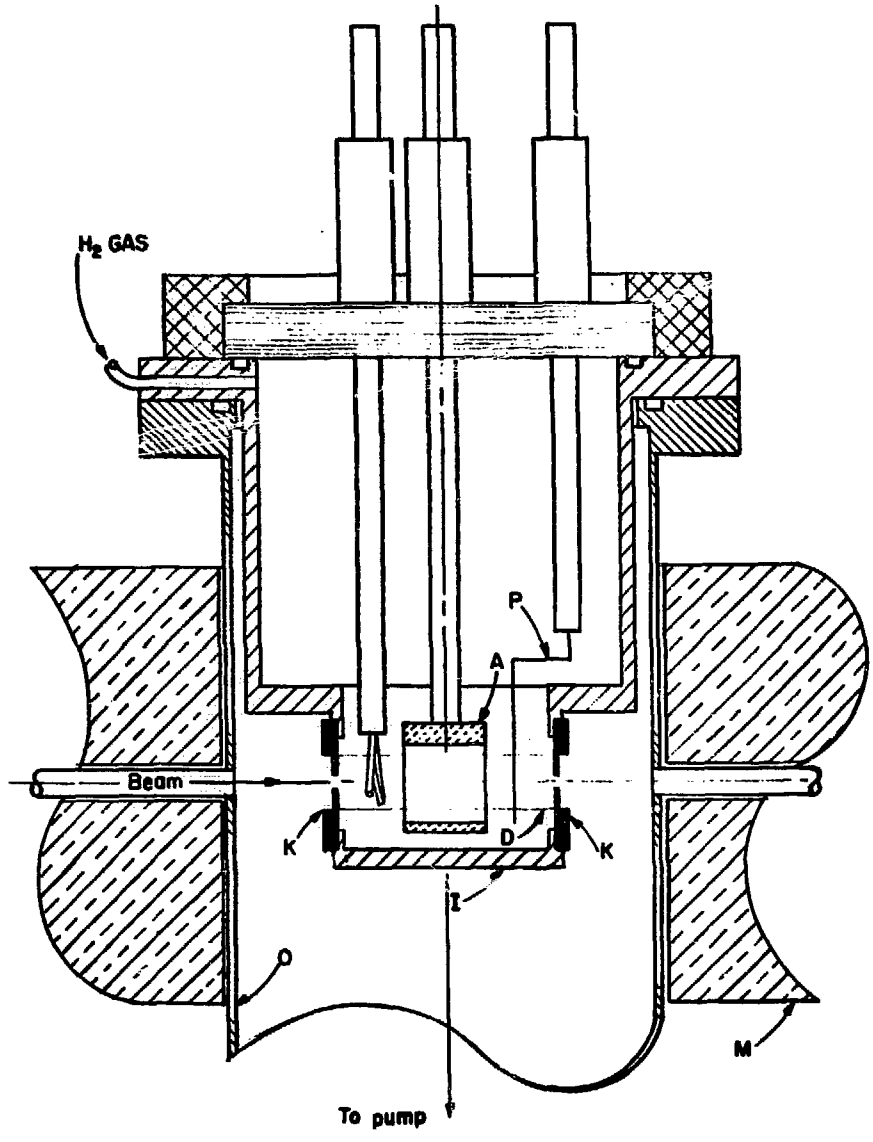

Fig. 15.
The plasma-stripping cross-section experiment. A, anode; D, plasma discharge; I, inner vacuum chamber; K, cathode disks; O, outer vacuum chamber; P, Langmuir plasma probe.

course of collecting the plasma stripping data, and are shown in Fig. 4.

B. Plasma Density Measurements

Use of a Langmuir probe, a small collecting electrode inserted into a plasma, to which various potentials can be applied so that the corresponding currents can be measured, is an important technique for measuring plasma properties. In a plasma, without a magnetic field and if the probe is small compared with the mean free path of the electrons and ions, the probe characteristic is of the general shape shown in Fig. 16. When a large negative potential is applied, all electrons are repelled and only positive ions are collected. This collected current reaches a saturation value I_i for large enough negative potentials. With increasing probe potential, the high-energy electrons begin to be collected, thus reducing the net positive-ion current. Eventually, a value V_f is reached at which there is zero net current to the probe. This is called the "*floating potential*"

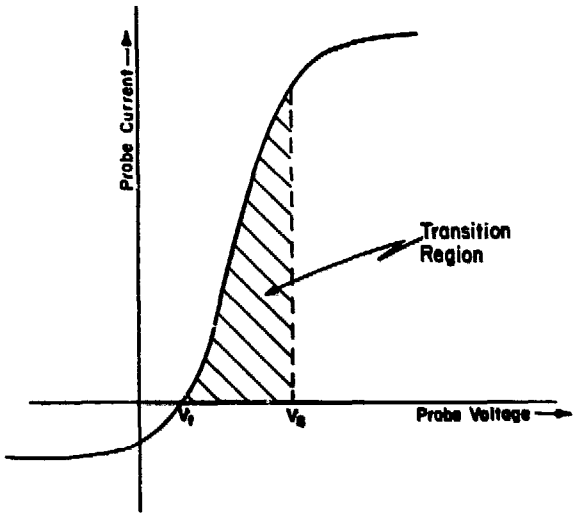

Fig. 16.
Typical Langmuir probe characteristics, the shape of the curve and the various parameters are described in the text.

because it is the potential assumed when an insulated electrode is inserted into the plasma. Further increase in the probe potential leads to the transition region where the negative current collected by the probe increases rapidly until a value V_s, the "space potential" is reached. At V_s, the probe is at the same potential as the plasma. There are no electric fields, and the charged particles migrate to the probe because of their thermal velocities. Because electrons move much faster than ions owing to their small mass, the probe collects predominantly electron current. If the probe voltage is made more positive, electrons are accelerated toward the probe. Also the ions are repelled and what little ion current was present at V_s vanishes when the saturated electron current I_{e_s} is reached.

If one can place a probe in the plasma so that it is not greatly disturbed, he can hope to get characteristic information about the plasma density n, electron temperature kT_e, and space potential V_s. The transition region shape is related to the distribution of electron energies and gives kT_e when the distribution is Maxwellian. The magnitude of the saturation electron current is a measure of $n(kT_e)^{1/2}$, from which n can be obtained. The magnitude of the ion saturation current depends on n and kT_e, but only slightly on kT_i, at least when $kT_i \ll kT_e$ as is usual. Hence, the ion temperature is not easily measured with a probe. Finally, the space potential can be determined by measuring V_f and calculating V_s.

Bohm, Burhop, and Massey[11] considered monoenergetic ions of energy 0.01 and 0.5 times kT_e. The dependence on the ion energy was slight, and the approximate result for the saturation ion current was

$$I_i = \frac{1}{2} n_i e A \left(\frac{kTe}{M}\right)^{1/2} , \tag{73}$$

where e is the electron unit of charge, A is the probe area, n_i is the plasma ion density, and M is the ion mass. In deriving this result, a "sheath edge" was approximated, so no dependence on probe voltage is given.

If the electron distribution is described by a Maxwellian distribution, Chen[12] has shown that the random electron current is given by

$$I_{e_s} = \frac{1}{2} n_e e A \left(\frac{2kT_e}{\pi m}\right)^{1/2} , \tag{74}$$

where n_e is the plasma electron density, which for plasma neutrality, is $n_e = n_i$, and m is the electron mass. Equation (74) gives the electron current to the probe at the space potential, V_s. As the probe voltage is made negative to V_s, the electron current is

$$I_e = I_{e_s} \exp\left(\frac{eV}{kTe}\right) . \tag{75}$$

If the electron current as a function of probe voltage is measured in the transition region, the electron temperature can be determined from

$$\frac{kTe}{e} = \left[\frac{d}{dV} \ln\left(\frac{Ie}{I_{e_s}}\right)\right]^{-1} . \tag{76}$$

When the probe voltage is decreased to V_f, the electron current and ion current cancel. Therefore,

$$\frac{eV_f}{kT_e} = \frac{1}{2} \ln\left(\frac{\pi}{2} \frac{m}{M}\right) . \tag{77}$$

Thus, for hydrogen, eV_f is about 3.5 times kT_e negative relative to the space potential. Therefore, by measuring V_f and determining kT_e, one can estimate the space potential.

Now that the electron temperature and the space potential are known, the plasma electron density can be calculated from Eq. (74). From Eqs. (73) and (74), we see that the ratio of the saturated electron current to the saturated ion current is

$$\frac{I_{es}}{I_i} = \left(\frac{2M}{\pi m}\right)^{1/2} . \tag{78}$$

So, for hydrogen, the saturated electron current is about 34 times the saturated ion current.

The foregoing discussion is applicable in the absence of a magnetic field. When a magnetic field is added, interpretation of the probe characteristic becomes far more difficult because the charged particles are constrained to gyrate about the lines of force with the Larmor radius

$$\rho = 1.445 \frac{\sqrt{ME}}{B} \quad , \tag{79}$$

where ρ is the Larmor radius (in mm), M is the charged particle's mass (in amu), E is the particle's energy (in eV), and B is the magnetic field (in kG).

The most noticeable effect of an applied magnetic field is the reduced electron saturation current. Whereas I_{e_s} is related to I_i by Eq. (78) in the absence of a magnetic field, this ratio falls by a factor of 10 to 20 when the Larmor radius of the electron is small compared to the probe and that of the ions remains large compared to the probe. Another effect of the magnetic field is to destroy the electron current saturation. That is, the probe current continues to increase with voltage as the electric field increases the plasma volume from which electrons can diffuse to the probe.

As for the transition region, it seems reasonable that the plot of $\ln I_e$ vs the probe voltage should still be linear when the distribution is Maxwellian, and that the slope should still give the electron temperature. If the magnetic field is so weak that the Larmor radius of the ion is large compared with the probe dimensions, the saturated ion current should still be described by Eq. (73).

Figure 17 shows a probe characteristic in our plasma cell. The electron temperature is determined from the slope of the linear part to be about

$$kT_e \approx 19 \text{ eV} \quad . \tag{80}$$

At this energy, the Larmor radius of the electron in the 1.5-kG magnetic field is

$$\rho_e = 0.002 \text{ mm} \quad , \tag{81}$$

much smaller than the 0.5-mm-diam probe. The Larmor radius of the ions in this field, assuming that the ion temperature

$$kT_i > 1 \text{ eV} \quad , \tag{82}$$

is

$$\rho_i > 0.96 \text{ mm} \tag{83}$$

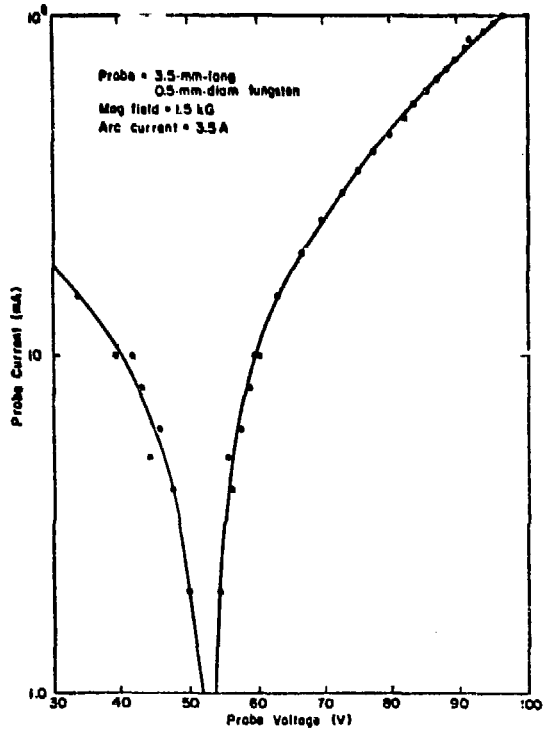

Fig. 17.
Typical Langmuir probe data from the plasma target used in the plasma-stripping cross-section experiment.

which is about twice the probe diameter. Therefore, the electron saturation current is strongly influenced by the magnetic field and cannot be used to determine the plasma density. However, using the saturated ion current, one can determine the ion density, using Eq. (73), to be about

$$n_i \approx 3 \times 10^{12} \text{ ions/cm}^3. \tag{84}$$

C. Neutral Gas Background

The most difficult problem in reducing the plasma-stripping data is caused by the unknown concentration of neutral hydrogen in the plasma. This problem results from at least two seemingly contradictory pieces of data.

- Langmuir probe measurements of the plasma operating under different arc conditions.

Measurements with a 1-A arc yield an ion density of 3.5×10^{12} ions/cm^3 and an electron

temperature of 1.7 eV. When the arc current was raised to 3.5 A, the ion density dropped slightly to 3×10^{12} ions/cm^3 and the electron temperature rose to 19 eV. At an electron temperature of 1.7 eV, only a very few electrons in the high-temperature tail of the distribution can ionize the neutral gas, whereas at 19 eV essentially all of the electrons can cause ionization. This behavior is what would be expected if essentially all the gas entering the plasma volume were ionized before it could escape. Then the increased electron temperature could not increase the ion density.

Gas can be excluded from the interior of the plasma in two obvious ways. First, a neutral particle could be ionized before passing through the plasma. At an electron temperature of 20 eV, the ionization length of a neutral H atom in a plasma of this density is about 2 cm,[13] and it is longer in the lower temperature plasma. The plasma column is only about 1.25 cm in diameter and 5 cm long, so a reasonable fraction of the neutral gas could pass completely through the plasma uneffected.

The neutrals also can be excluded from the interior of the plasma by its electron pressure and by heating. At $T_e = 2$ eV, the electron pressure is about 6×10^{-3} torr, and at $T_e = 20$ eV it is about 6×10^{-2} torr. In both cases, the neutral gas pressure outside the plasma is 8×10^{-3} torr. Unfortunately, again, the path length that a neutral can penetrate into the plasma before it collides with an electron is comparable to the plasma diameter.

Obviously both effects occur, that is, collisions that ionize neutral and those that do not. The latter cause heating and exclusion of the neutrals from the interior.

- The second piece of data, which implies a modest neutral density within the plasma, is the rate of particle flow out of the plasma cell.

The gas supply to the plasma cell injects a constant number of H_2 molecules per second into the inner vacuum chamber. The flow out of this chamber must equal the flow in, or the pressure would rise indefinitely. Because the chamber exits are covered by the plasma, neutral gas flowing from the chamber must pass through the plasma. The Langmuir probe measurements permit calculating the number of ions passing through the chamber exits. Such a calculation indicates that about 1/3 of the particles leaving the chamber can be accounted for by ion flow and the remaining 2/3 must be neutral particles. The only way to maintain this flow with a reduced neutral density is to raise the neutral temperature. The plasma certainly does this, but to what extent has not been determined.

At present it is impossible to make a reasonable estimate of the neutral density within the plasma, so we can only estimate the plasma stripping on the basis of "reasonable" assumptions. At each incident H^- energy, two cross sections are calculated. The higher value assumes that the neutral gas density in the center of the plasma is essentially zero. The lower value assumes that it is 25% of the neutral density when the plasma is not present. This corresponds to a neutral H_2 temperature of about 1850° C (0.18 eV) in the plasma center. These points are plotted in Fig. 4 as open circles joined by bars at 3, 4.5, and 6 MeV, with the further assumption that the stripping cross section from the plasma ions equals that of the plasma electrons. Work continues to determine the neutral gas background in these measurements.

X. HIGH-CURRENT, HIGH-BRIGHTNESS, H^- ION SOURCE DEVELOPMENT PROGRAM

A. Goals

During the past fiscal year, a program for development of high-current, high-brightness, negative hydrogen (H^-) ion sources has been initiated. The objective is to demonstrate the feasibility of an ion source that can produce an H^- current of about 100 mA, with a normalized two-dimensional emittance (ϵ) of less than 0.02 π cm-mrad. The desired beam duty factor (df) is about 10%.

B. Terminology

In addition to ion current, which needs no elaboration, the beam parameters used here are as follows. (1) The two-dimensional normalized emittance in a plane perpendicular to the beam direction,

$$\epsilon_x = \beta\gamma \iint dx dx' \quad \text{(cm-mrad)} \quad , \tag{85}$$

where β and γ are the usual relativistic quantities and the integral is the phase space (x,x') area occupied by a designated fraction of the beam particles. Expressed thus, this quantity represents the amount of transverse disorder in the ion beam, and it is invariant with respect to beam energy. (2) The normalized brightness,

$$B = \frac{2I}{\epsilon_x \epsilon_y} \quad , \qquad (86)$$

where I is the ion current and ϵ_x and ϵ_y are the normalized emittances in the (x,x') and (y,y') phase planes (the z-axis conventionally being taken along the beam direction). This quantity is just the particle density in four-dimensional phase space, and it is a more significant indicator of ion source performance than I or ϵ taken separately, as it is characteristic of the ion formation process. In terms of the previously stated ion current and emittance objectives, the desired H^- ion source brightness is $B = 5 \times 10^{11}$ A/m^2-rad^2, or greater. (3) The beam duty factor, df, which is just the percentage of the time the ion source is producing an H^- beam.

C. Background

Two main approaches to H^- ion source development could lead to devices having the desired performance levels. These are the charge exchange method in which an intense proton (H^+) beam is fractionally converted to H^- beam in a suitable charge-adding medium, and the direct extraction method, in which H^- ions are generated by a surface emission process associated with a discharge (arc) in hydrogen gas.

The first method has been used for many years, with H_2 as the charge exchange medium, at several accelerator installations (including LAMPF), for production of moderate H^- currents.[14] With development of high-current, low-energy, positive ion sources for the Controlled Thermonuclear Reactor (CTR) program, it has become possible to take advantage of the alkali metal vapors as charge exchange media. They convert H^+ ions to H^- ions very efficiently at beam energies of 0.5-5.0 keV. A current of up to 50 mA of negative deuterium ions (D^-) has been produced at Lawrence Livermore Laboratory (LLL) with 100% duty factor, using cesium as the charge exchange medium.[15] However the estimated D^- beam emittance has the large value of 0.25 to 0.5 π cm-mrad. More recently, a group in the USSR has reported production of a 70-mA H^- beam with an emittance (averaged over x,x' and y,y' spaces) of 0.05 π cm-mrad.[16] Unfortunately, the present duty factor of this pulsed source is very low, less than 0.1%. The direct extraction surface emission technique has lately been developed by the Novosibirsk group in the USSR to yield very large H^- currents.[17] With one exception, most of these ion sources operate at very low duty factors and have relatively large emittances (0.2 to 0.3 π for 25 mA, for example). A Penning-type surface emission ion source developed by Dudnikov,[18] on the other hand, has produced H^- currents of up to 150 mA with an emittance of about 0.06 π cm-mrad, or less. (This corresponds to a brightness of 0.84×10^{11} A/m^2-rad^2.) The reported duty factor of this source is 3%. Although the operation of surface emission ion sources is not well understood, it is generally accepted that H^- ions are emitted from the ion source cathode surface and accelerated to energies of 150 eV near the anode where they exchange with H^0 atoms, thereby forming slow H^- ions. At least two models have been suggested for the surface H^- emission mechanism, a process greatly enhanced by the presence of cesium.[19,20]

The ultimate performance capability of surface emission ion sources is probably less well understood than that of charge exchange sources. However, our understanding of the latter is far from comprehensive. It is not clear which kind of H^- ion source will eventually be able to meet the performance requirements, and both approaches should be developed in parallel, if possible. The Dudnikov surface emission source appears closer than any other device to all of these performance levels. However, with proper design of the H^+ generator and extraction system,[21] the charge exchange technique can provide beams of similar intensity and emittance.

During the past year, a charge exchange ion source test stand has been completed and measurements on ion beam parameters have begun. This program was implemented in 1972. Its original goal was to develop a 20-mA H^- ion source (with an emittance and duty factor matched to the LAMPF linear accelerator) to determine the feasibility of the central concepts involved in the WNR high-current proton storage ring proposal.[22] This proposal calls for H^- charge-stripping injection into the storage ring and beam-bunching to be carried out in the ion source. A charge exchange source seemed most suitable for meeting these requirements.

Most of the equipment for this test stand was purchased and assembled before July 1974. Construction has been completed, and the ion beam measurement program has been in progress since then. A second test stand, for development of a surface emission H^- ion source of the Dudnikov type is in the design stage. Most of the ion source effort during the next fiscal year will be devoted to building this test stand.

In the following sections, we describe the charge exchange scheme in general, the charge exchange H^- ion source test stand, beam-measuring instrumentation, experimental results to date, and

future plans for charge exchange ion source development. Plans for, and the status of, the surface emission source program are discussed in the final section.

D. Charge Exchange Ion Source Scheme and Choice of Exchange Medium

The charge exchange approach to H^- beam production can be outlined as follows. A high-current H^+ ion beam is generated at a suitable energy by a discharge plasma and extraction system. The generation of large beams in the low-energy (keV) range requires devices that have large extraction areas and closely spaced multiple-aperture, or gridded, (acceleration and deceleration) extraction electrodes. This is a consequence of the Child, Langmuir, and Schottky law governing the relation between the space-change limited extracted ion current and the parameters of the extraction geometry.

$$I = \frac{4A\epsilon_0}{9}\left(\frac{2e}{m}\right)^{1/2}\frac{V_0^{3/2}}{d^2}\ \text{amperes/m}^2\ , \qquad (87)$$

where I is total extracted ion current; A, the area of the extraction electrodes; d, the electrode spacing; and V_0, their potential differences, and e/m and ϵ_0 have their usual meanings. The H^+ beam is projected through a windowless thin gas or vapor target, where part of it is converted to H^- beam by one of the following processes.

$$\begin{aligned}
&H^+ + X \rightarrow H^0(1S) + X^+ \ , \\
&\qquad H^0(1S) + X \rightarrow H^- + X^+ \ , \\
&H^+ + X \rightarrow H^0(2P) + X^+ \ , \\
&\qquad H^0(2P) \rightarrow H^0(1S) + \nu(1.6 \times 10^{-9}\text{s}) \ , \\
&\qquad\qquad H^0(1S) + X \rightarrow H^- + X^+ \ , \\
&H^+ + X \rightarrow H^0(2S) + X^+ \ , \\
&\qquad H^0(2S) + E(z,t) \rightarrow H^0(1S) + \nu \ , \\
&\qquad\qquad\qquad H^0(1S) + X \rightarrow H^- + X^+ \ .
\end{aligned} \qquad (88)$$

Here X represents the target atom, ν the characteristic photon resulting from the 2P-1S transition in H^0, and E(z,t) the electric field present in the beam because of space charge and/or externally applied potentials. Whether the process goes through the H^0 ground state or its first excited state depends on the difference $|\Delta E|$ between the internal energies of initial and final configurations, the reaction having the smaller $|\Delta E|$ being favored. After emerging from the charge exchange cell, the H^- beam is accelerated and focused by an electrostatic lens system. For accelerator application, it would then be suitably matched to the high-gradient column of a Cockroft-Walton injector, accelerated to the desired injection energy, and transported to the linac.

The basic choices in development of a practical charge exchange H^- source are the kind of H^+ generator to use, and the charge exchange material to select. Because of the variation in optimum H^+ energy and $H^+ \rightarrow H^-$ conversion efficiency of possible charge exchange media, these choices are closely coupled. We have chosen to concentrate on the alkali metal vapors, particularly cesium and sodium, which have maximum conversion efficiencies at beam energies of 0.5-5 keV. This choice has dictated selection of an H^+ injection system optimized for low-energy operation, which at present is a multiple-aperture, reflex-arc duoplasmatron of the LLL MATS II type.[23] For low H^+ beam emittance, this is not the ideal source in its present form. However, it was readily available, and originally represented a convenient way of starting a charge exchange H^- beam program. We probably should replace it at a suitable time with a device like the Lawrence Berkely Laboratory (LBL) H^+ source,[24] which seems at least five times brighter, or perhaps an H^+ source like that of the Novosibirsk group.[21]

Table V compares the relative suitability of the common alkali vapors and the more conventional H_2 as charge exchange media for H^- ion production. The second column lists the maximum equilibrium H^- fraction (F^-_∞) after traversal of the medium; the third column, the H^+ beam energy (E_m) corresponding to the maximum; the fourth column, the H^+ current required $I(H^+)$ at E_m for 100 mA of H^- ions; and the fifth column, the minimum power $P(H^+)$ the extraction system requires to generate this beam. The data for F^-_∞ and E_m were obtained from Ref. 25 for lithium, sodium, potassium, and cesium. The bracketed F^-_∞ and E_m data for cesium are those of Ref. 26, which are not inconsistent with those of Ref. 25, as they represent an extension to lower H^+ energy.

Use of any alkali vapor as the charge exchange medium represents an enormous savings in the power needed to produce the initial H^+ beam, compared with use of H_2. Actually, this is a very conservative estimate, as the additional power in the

TABLE V

Target	F^{∞}_{-}	E_m (eV)	$I(H^+)$(mA)	$P(H^+)$(W)
Li	0.06	3 500	1 665	5 825
Na	0.12	2 500	830	2 080
K	0.14	1 300	710	925
Cs	0.21	750	475	355
	(0.26)	(400)	(385)	(150)
H_2	0.02	15 000	5 000	75 000

discharge (much greater for the large H^+ currents needed in the H_2 case than for the alkalis) has been neglected. Cesium is by far the most efficient $H^+ \rightarrow H^-$ converter. However, it suffers from the fact that very low beam energy is required to achieve this efficiency, and the $V^{3/2}$ factor in Eq. (87) makes it difficult for the H^+ source to supply large enough currents. Sodium vapor, whose efficiency ($H^+ \rightarrow H^-$) is 0.12 at a much higher beam energy (2.5 keV) is probably a more satisfactory charge exchange medium. Furthermore, the peak of the energy dependence curve of F^{∞}_{-} for sodium is broad compared with that for cesium; the conversion efficiency does not fall below 0.10 for H^+ beam energies up to 5 keV. The equilibrium fractions F^{∞}_{-} have been plotted in Fig. 18 as a function of beam energy, for cesium and sodium.

A number of other factors enter the picture, in addition to those implied or explicit in Table V. The most important is the brightness or four-dimensional phase space density $B = 2I/\epsilon_x\epsilon_y$ of the H^- beam produced in the charge exchange process, where ϵ_x and ϵ_y are the normalized areas in (x,x') and (y,y') space occupied by a beam of current level I. The output current of the MATS II source (for a given extraction and collection geometry) depends on extraction voltage roughly as $V^{3/2}$.[23] Because the apparatus geometry is fixed, the unnormalized "acceptance" areas $\epsilon_x/\beta\gamma$ and $\epsilon_y/\beta\gamma$ are independent of beam energy, and the normalized four-dimensional emittance is proportional to $(\beta\gamma)^2$. The H^+ beam brightness then varies approximately as

$$B(H^+) \sim \frac{V^{3/2}}{(\beta\gamma)^2} \sim \frac{V^{3/2}}{V} = V^{1/2} \quad . \tag{89}$$

Neglecting the scattering in the $H^+ \rightarrow H^-$ conversion process, the resulting H^- beam brightness varies as

$$B(H^-) \sim (F^{\infty}_{-})B(H^+) = F^{\infty}_{-}V^{1/2} \quad . \tag{90}$$

From Table V, the values of this relative brightness factor (arbitrary units) are: Li, 3.5; Na, 6.0; K, 5.0; Cs, 5.8; and H_2, 2.4. The value for sodium at E = 5 keV (where $F^{\infty}_{-} = 0.10$) rises to 7.0.

Given the goal of maximizing both H^- intensity and beam brightness without excessive power consumption, the previous considerations suggest that sodium is the optimum charge exchange medium. However, for experimental reasons, the first measurements on the prototype charge exchange source have been conducted using cesium.

E. Charge Exchange H^- Source Test Stand

The essential components of the charge exchange ion source test stand are indicated in Fig. 19. More detail is shown in Fig. 20, a photograph of the test stand, with the first vacuum chamber open. These

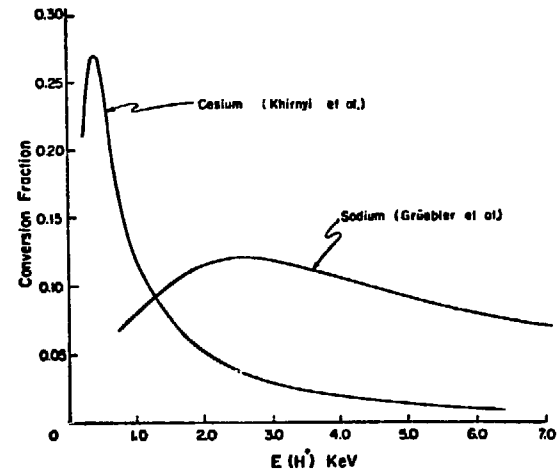

Fig. 18.
F^{∞}_{-} vs H^+ beam energy for cesium and sodium. Data are from Refs. 25 and 26.

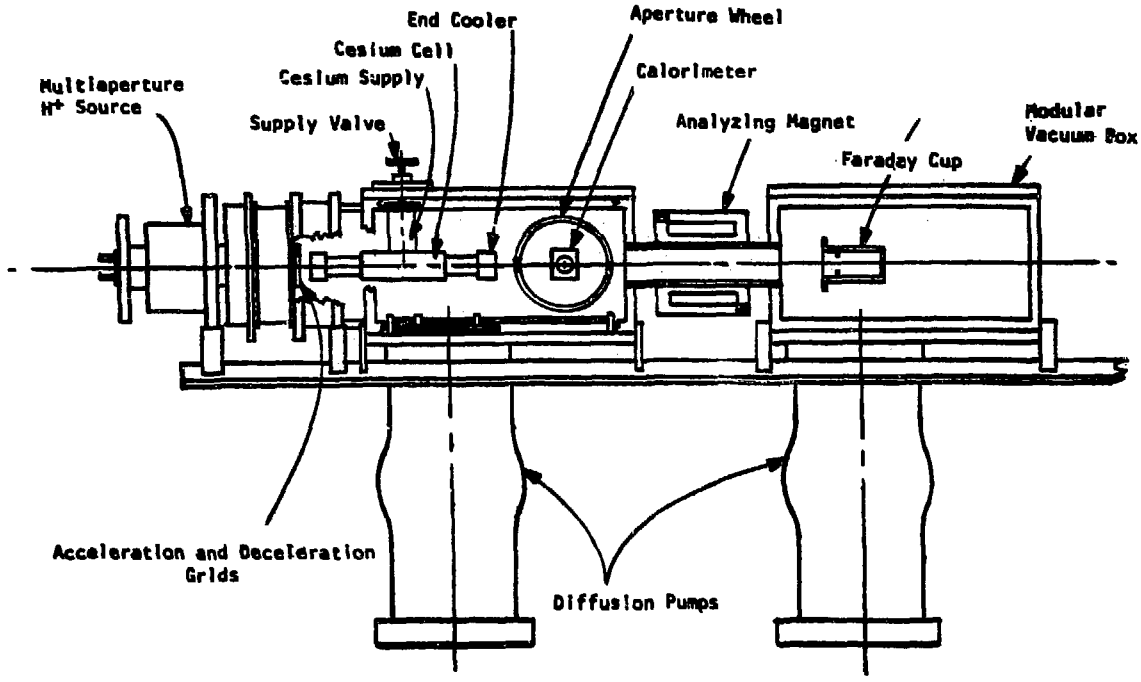

Fig. 19.
The charge exchange H^- ion source test stand.

figures show the test stand configuration for the first set of experiments. Major changes have been made in the beam-measuring instrumentation, but the basic apparatus layout is that shown.

The positive ion generator is a LLL MATS II-type multiple aperture ion source, whose construction and performance characteristics have been described in the literature.[23] The machined copper plasma grid and acceleration and deceleration grids incorporate 279 holes in a hexagonal array with 0.27 cm between centers. Hole diameters are: plasma grid, 0.16 cm; acceleration grid, 0.20 cm; and deceleration grid, 0.16 cm. The plasma-forming region is operated at extraction potential relative to ground, supplied by electronics located in an insulated rack powered by a 20-kVA isolation transformer. A uv window in the vacuum wall between the anode and plasma boundary grid permits spectroscopic observation of the plasma in this region.

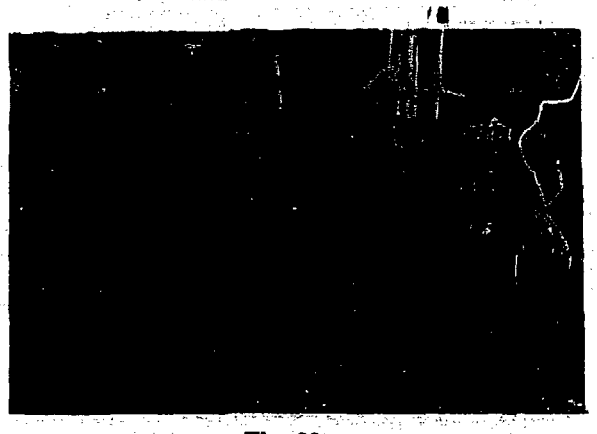

Fig. 20.
The ion source test stand showing H^+ generator, charge exchange cell, and beam calorimeter.

The vacuum system to which the MATS II source is coupled is modular and consists of rectangular steel frames covered by demountable aluminum plates on four sides. All experimental hardware is mounted on these plates, permitting flexibility in altering the configurations of diagnostics, etc. Each vacuum box is pumped by a single 2400-ℓ/s diffusion pump through a water-cooled chevron baffle.

The alkali vapor charge exchange cell is designed for use with either cesium or sodium. Construction details are shown in Fig. 21, a photograph of the unit mounted on its supporting plate. The system is basically a heated and valved stainless steel reservoir (25-g capacity for cesium) and a recirculating charge transfer cell. The cell is a 3.2-cm-i.d. stainless steel tube, 36 cm long, containing three layers of No. 160 stainless steel mesh pressed into its interior surface. The central 15 cm, clamped in a copper block heated by coaxial heater wire, can be raised to

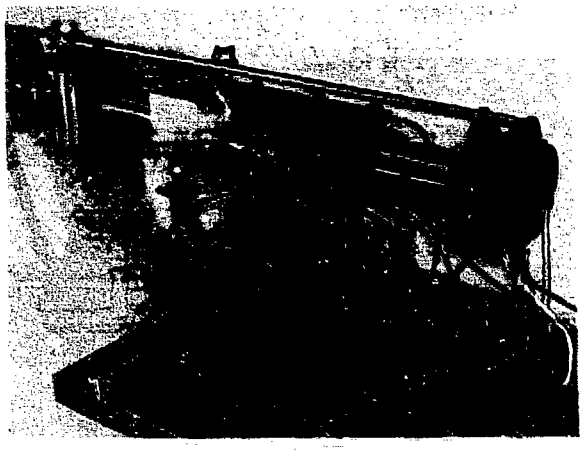

Fig. 21.
Alkali vapor charge exchange cell and supply reservoir mounted on vacuum box lid.

250°C. The ends of the steel tube are clamped in independently heated (or cooled) copper blocks used to keep them at a temperature slightly above the solidification point (29°C for cesium, 98° for sodium). The central region is run using liquid alkali metal in the mesh in equilibrium with its vapor at a temperature high enough to provide adequate target thickness for optimum $H^+ \rightarrow H^-$ conversion. As the vapor moves toward the ends of the cell, it condenses on the cooled walls and is returned by capillary action in the mesh to the central region. This recirculating technique should reduce loss of alkali vapor from the cell by a very large factor (up to 1000), thus minimizing contamination of the vacuum system, electrical breakdown of the extraction system, and consumption of the alkali metal.[27]

F. Beam Measurement Instrumentation

During initial measurements, the beam instrumentation was arranged as follows. A combined Faraday cup and calorimeter 20 cm downstream from the cesium cell measured the total beam current and power transmitted through the charge exchange medium. The collector throat was large enough to collect all the particles passing through the cell. Beam power was determined by measuring the temperature rise in the metered water flow which cooled the collector. Assuming that all positive ions H_1^+, H_2^+, and H_3^+ extracted from the MATS II plasma were accelerated to the same energy by the acceleration and deceleration system, we could infer the equivalent particle current transmitted by the cesium cell.

The total beam collector was isolated from ground and guarded by a bias ring held at −200 V. It could therefore be used with reasonable confidence for direct current measurements. However, these measurements required further interpretation, because, under given operating conditions, the beam contained unknown proportions of neutral, positive, and negative particles.

This charge state composition information was provided by a magnetic differential analyzing system in the second vacuum chamber. In this configuration, the calorimeter was retracted, and a 1-mm aperture was scanned horizontally across the beam. The beam pencil this collimator defined was then passed through a uniform-field electromagnet that separated it into positive, neutral, and negative components. In addition to the full-energy H_1^+, H_1^0, and H_1^- fractions, there were also the H_2^+ and H_3^+ beams, and the 1/2 and 1/3 energy positive, negative, and neutral beams arising from charge exchange and dissociation of these species in the cesium vapor and the background hydrogen gas. The negative and positive components were deflected by 30° into two electrostatically guarded Faraday cups. The neutral component was incident on a negatively biased clean copper flag, and it was measured by secondary electron emission from this surface. The neutral detector provided only relative measurements owing to the difficulties inherent in absolute calibration. It could be rotated out of the way, permitting the beam to strike a Pyrex window at the end of the second vacuum chamber. The induced fluorescence at the glass surface permitted a rough estimate of the beam pencil diameter at this point.

After the first series of beam tests, the instrumentation was rebuilt to permit more accurate determination of total current and power and greater flexibility in beam profile and charge analysis measurements, and to permit emittance measurements to be made. The original calorimeter and Faraday cup was replaced by an improved version located inside the spool that connected the two vacuum chambers. The rear of the new cup contained a power resistor for accurate *in situ* power calibration of the calorimeter. Two 0.5-mm apertures could be scanned horizontally across the beam, one in front of, and one behind the Faraday cup. Either of these apertures, driven by micrometer-adjustable linear actuators, could be used for beam profile measurements. Used together, they made emittance measurements in the following manner.

With the front aperture fixed at some horizontal position x_a, the beam pencil thus transmitted was scanned in the same plane by the rear aperture to measure x_a'. The front aperture was then moved to a

new position x_b, and the rear aperture was scanned as before to measure x_b'. By repeating this procedure for a suitable number of front aperture positions, and plotting the x,x' points obtained, one could construct the beam phase space envelope.

G. Charge Exchange Source Test Results

The charge-exchange H^- source was tested with cesium as the charge-exchange medium in two series of beam measurements. In the first series, using instrumentation described in the previous section, we observed a maximum H^- beam of 10 mA. No emittance measurements were made. The source was operated cw (steady state), and typical operating parameters were:

Arc current: 30 A,
H_2 gas flow: 27 cm^3/s (STP),
Extraction voltage: 2100 V,
Beam energy: 1600 eV,
Extraction supply load: 450 mA,
Beam power through cesium cell: 35 W.

Before introducing cesium vapor, we measured the positive ion beam charge state composition and found it to be typically 25% H_1^+, 70% H_2^+, and 5% H_3^+. At first glance, the low percentage of H_1^+ seemed an undesirable source characteristic. However, it later became clear that the large H_2^+ component could be used advantageously to produce a larger H^- beam than might have been obtained if the H_1^+:H_2^+ ratio were reversed. When the H_2^+ beam is used to generate H^- ions in the charge exchange medium, it first breaks up into two half-energy particles. For these particles to have the correct energy for maximum H^- formation, the H_2^+ ions must be extracted from the positive ion source with twice the energy required for H_1^+ ions. Because of the $V^{3/2}$ factor noted earlier, this fact allows more positive ion current to be projected through the charge exchange cell. Also, as each H_2^+ ion breaks up to form two half-energy particles in the cesium cell, an additional factor of 2 in beam intensity is gained.

We had difficulty in sustaining the acceleration and deceleration system electrode potentials when the cesium cell was turned on. This seemed to be due partly to the cesium cell's proximity to these electrodes (1.5-cm spacing), and partly to faulty operation of the cesium supply valve. Hydrogen pressure in the first vacuum chamber was high, usually about 2×10^{-4} torr, when the source was running.

Before the second test series, we made several changes in the test stand. These included: doubling the H_2 pumping speed in the first vacuum chamber, remounting the cesium cell 15 cm from the acceleration and deceleration grids, and upgrading the beam measurement instrumentation as described in Sec. F.

In the second test series, H^- beams of up to 6 mA were measured in the new total beam calorimeter and Faraday cup. H^- beam profile measurements were made using the front scanning aperture. A typical profile is shown in Fig. 22. The beam intensity is fairly uniform across the central 2/3 of the beam and drops sharply as the diameter of the cesium cell is approached. The intensity dip near beam center, which was not always present, could be explained in several ways. Because there are too few data to back up any of the possibilities, that feature is not discussed further.

Using the method described in Sec. F, we made several (x,x') emittance measurements on the H^- and H^0 beams. Data typical of a 5-mA H^- beam are shown in Fig. 23. Using symmetry arguments, whose validity we checked in other runs, we drew an ellipse-like curve through the x,x' data points. It represents the boundary of a phase space area containing ~90% of the H^- beam. The normalized H^- beam emittance, $\beta\gamma\iint dx dx'$, derived from Fig. 23 is 0.12 π cm-mrad. This should be compared with the existing LAMPF H^- source which has an emittance of 0.16 π cm-mrad, and 20 times less intensity. The brightness of the tested beam is 6.7×10^9 A/m^2-rad^2.

The H_2^+ beam energy that gave maximum H^- formation was 1250 eV, corresponding to 625-eV energy for the H^0 particles participating in the H^--forming collisions in cesium. Coupled with the total beam (power) measurements, and the previously determined H_2^+ ion fraction produced by the MATS

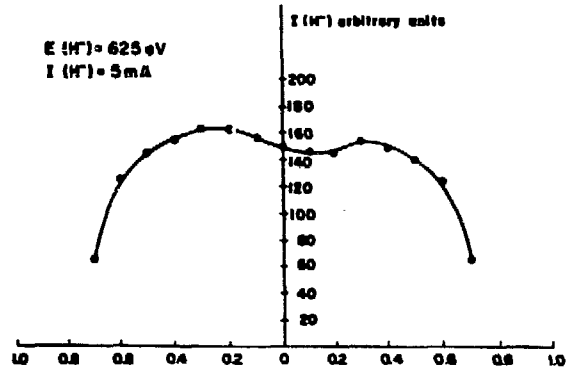

Fig. 22.
H^- beam profile. Abscissa is distance from beam center, in inches.

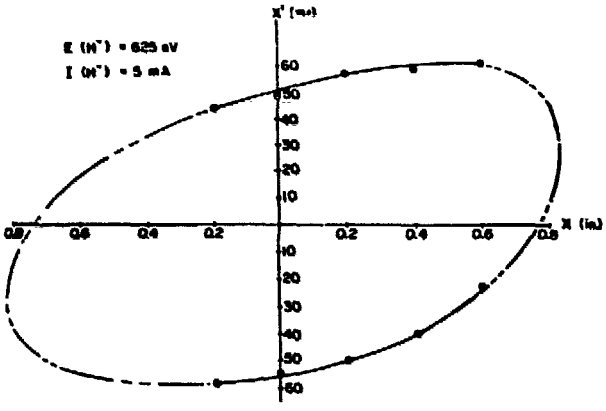

Fig. 23.
H^- beam emittance measurement in (x,x') space at 625 eV.

II source, the observed H^- yield indicated a nominal H^-/H^+ conversion efficiency (F^{∞}) of about 0.23, in very good agreement with the charge exchange data of Ref. 26.

Beam power measurements made with the calorimeter should have no more than a 10% uncertainty. Within the limits of indicator readability, the flow meter measurements agreed with those based on the power resistor calibration. Total H^- current measurements are thought to have a similar level of certainty. We ran several tests to confirm and cross-check the H^- current readings, to eliminate the possibility that the measured currents were actually due to electrons trapped in the beam or to a variety of other causes. All these tests had essentially negative results.

The H^- currents so far obtained with the charge exchange source are consistent with those of Ref. 15, when proper allowance is made for the difference in charge exchange cell areas (factor of 4), and beam particles (H^- instead of D^-). The measured H^- emittance is better than that estimated for the Ref. 15 ion source configuration. Although the test results are far short of the desired H^- performance goals, the device on our test stand is the brightest cw H^- ion source operating in the U.S. No pulsed, low-duty-factor H^- source in this country is appreciably brighter.

H. Further Plans for Charge Exchange Source Development

During the last beam measurement series, cesium vapor control continued to be troublesome. Cesium cell temperature and feed control are being refined. Other improvements are being incorporated in the beam measurement instrumentation. When these are completed, we plan a third test series with cesium vapor. Later, we plan to replace cesium with sodium, which should provide a more intense, brighter H^- beam. We will make current intensity, profile, and emittance measurements like those described in Sec. G. We may want, at some point, to accelerate the H^- beam to higher (50-keV) energy, partly to eliminate uncertainties in the beam measurements, and partly to investigate how a charge-exchange H^- source can be engineered realistically for installation in an accelerator injector.

Clearly, to brighten the charge exchange H^- source much, we will have to replace the existing MATS II positive ion injector with a brighter device. This could be an appropriately scaled version of the magnetic-field-free LBL H^+ source,[24] or a source like that of Ref. 21. The very high brightness of the latter apparently results from the absence of magnetic fields in the plasma-forming region and a unique extraction geometry based on closely spaced, very fine, wire and ribbon grids that have extremely high alignment tolerances and 90% transparency. Although this source is now used only in very low duty factor operation, preliminary calculations suggest that it should be capable of duty factors approaching 10%. As noted earlier, this source operating with a sodium vapor charge exchange cell has produced H^- beams of 70-100 mA with an emittance of 0.05 π cm-mrad.

Although the principal effort in the H^- beam development program during the next fiscal year will be on the surface emission ion source (as discussed in the following section), the charge exchange source work will be extended at least to the sodium measurements noted above. After that, a decision will be made to suspend charge exchange work or to develop a suitably bright H^+ injector.

I. Surface Emission Ion Source

Various kinds of surface emission, cesium-injected, H^- ion sources have been developed recently in the USSR. The three basic types are the planotron source which has a magnetron-type electric and magnetic field arrangement,[17] the hollow-arc duoplasmatron in which the electric and magnetic fields are coaxial,[28] and the source developed by Dudnikov, which has a Penning-type geometry.[18] The first two generate large H^- currents but appear to have a relatively low brightness. The Penning source, on the other hand, seems ideally suited to accelerator application, and

has a reported H^- current of 150 mA, an emittance of less than 0.06 π cm-mrad, and a 3% duty factor.

Although the exact mechanism for H^- formation is not understood, it is generally conceded that all surface emission sources work roughly as follows. Negative ions are produced at the cathode surface and accelerated, by the cathode and anode potential difference, to the anode region. Here, these 100- to 200-eV H^- ions charge exchange with H^0 atoms produced by the discharge to yield slow H^- ions. In all source geometries except the Penning geometry, both slow and fast H^- ions are extracted at the anode aperture, thus building into the beam a transverse energy spread of at least 100 eV. Owing to the arrangement of electric and magnetic fields and the extraction aperture in the Penning source, only the slow H^- ions are accelerated, so a very low emittance H^- beam is produced.

Using the none-too-clear Russian drawings in Ref. 18 (shown as Fig. 24), information brought back by U.S. visitors to the Novosibirsk ion source laboratory, and considerable deduction and inference, we have assembled a plausible picture (Fig. 25) of how the Dudnikov source is constructed. A LASL version of the source now being designed should be assembled during the next three months. During this period, we also plan to assemble the test stand for the ion source and partially complete the vacuum system and beam measurement instrumentation.

Some capital equipment for this program has been bought. The rest will be purchased after July 1. We are developing a transistor-switched, high-current, pulsed-arc supply (300-A and 200-V) to run the discharge. Preliminary results are promising.

During the second and third quarters of the fiscal year, we expect to complete the vacuum system, beam diagnostics, and electrical systems of the test stand. Hopefully, by the end of the third quarter, the surface emission H^- source will be essentially complete. If we can meet this schedule, we will devote the fourth quarter to initial beam tests.

ACKNOWLEDGMENTS

It is impossible to acknowledge properly all who contributed to this work. However, we are grateful to R. B. Perkins, E. A. Knapp, M. S. Moore, R. G. Fluharty, and J. A. Farrell for their helpful discussions, assistance, and encouragement during various stages of this work. Special thanks are due to W. Coelho for his skillful design, drafting, and liaison with the shops and Zia crafts. Our technicians, R. D. Clayton, M. Smith, D. Hoover, and Mrs. K. Hughes performed superbly, working many hours of overtime when required and expressing a strong interest in the successful completion of the experimental work.

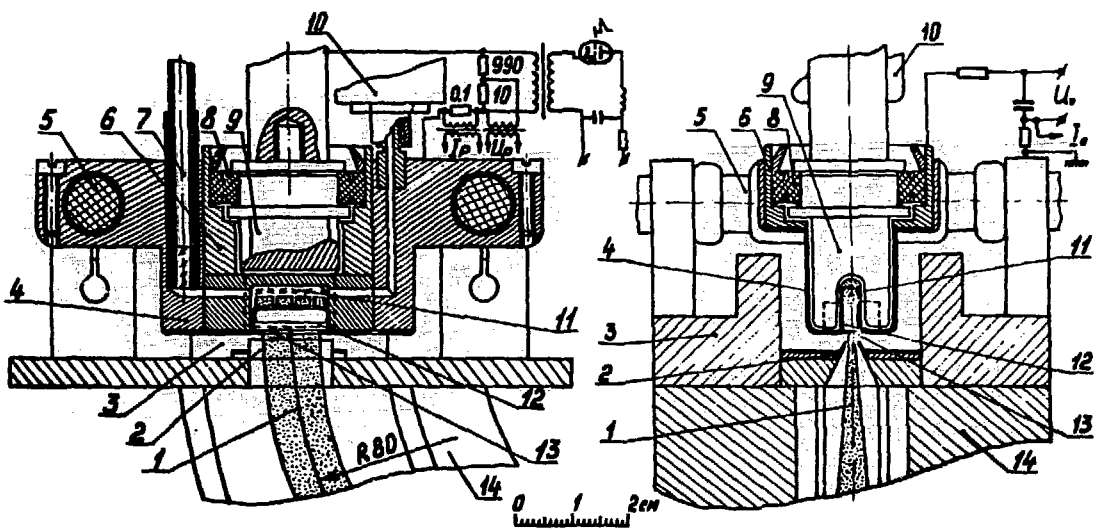

Fig. 24.
Views of the Penning Ion Source taken from Ref. 18.
1, negative ion beam; 2, extracting electrode; 3, magnet poles; 4, discharge chamber; 5, high-voltage insulator; 6, anode insert; 7, cesium input channel; 8, partition insulator; 9, cathode; 10, gas valve; 11, anode with cavity for cesium; 12, anode groove; 13, emission slit; and 14, analysing magnet.

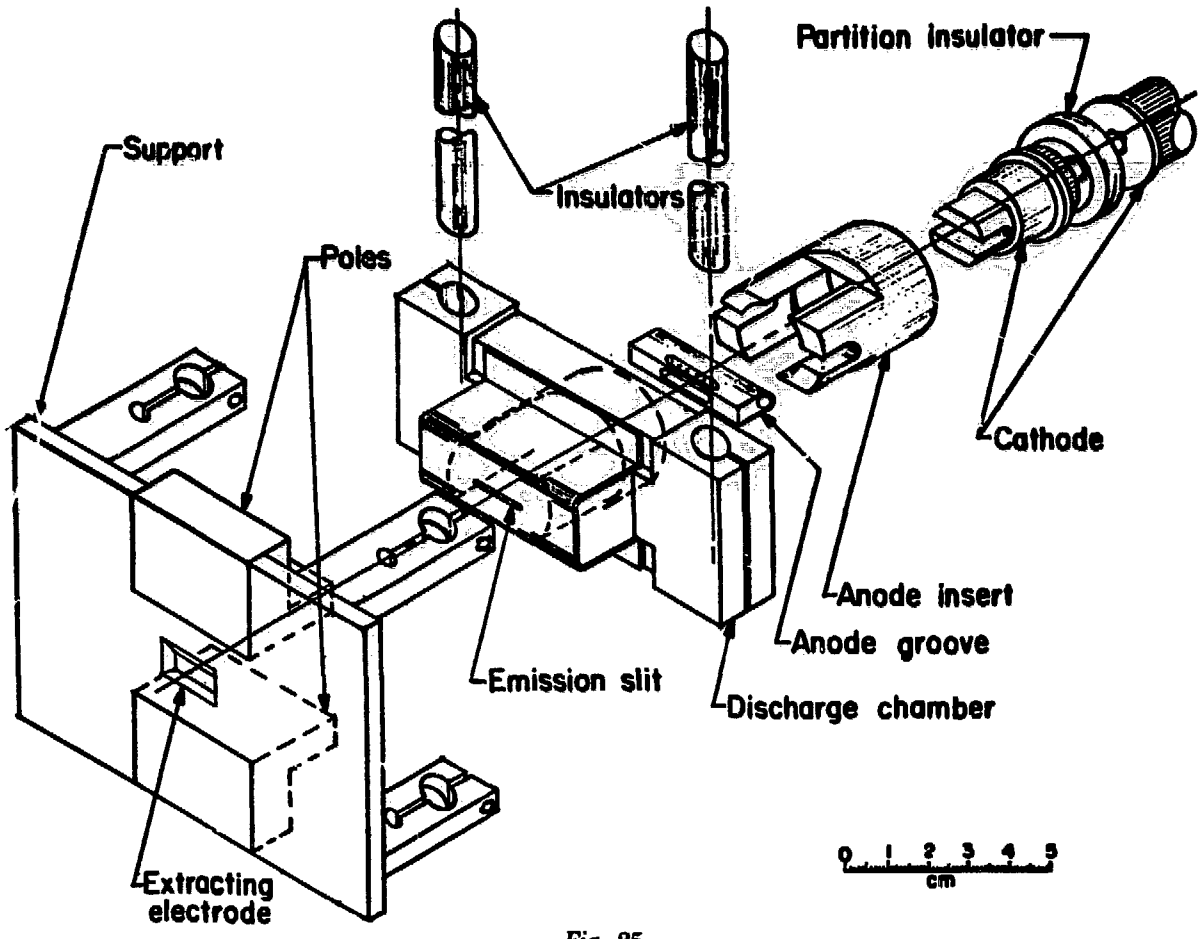

Fig. 25.
LASL reconstruction of the Penning source.

REFERENCES

1. R. Smythe and J. W. Toevs, "Collisional Electron Detachment from Hydrogen Atoms and Negative Hydrogen Ions between 4 and 18 MeV," Phys. Rev. **139**, 1A, 15 (1965).

2. S. K. Allison, "Experimental Results on Charge-Changing Collisions of Hydrogen and Helium Atoms and Ions at Kinetic Energies above 0.2 keV," Rev. Mod. Phys. **30**, 1137 (1958).

3. K. H. Berkner, S. N. Kaplan, and R. V. Pyle, "Collisional Electron Detachment from 20 MeV D^0 and D^- Ions," Phys. Rev. **134**, 6A, 1461 (1964).

4. D. G. Dance, F. M. A. Harrison, and R. D. Rundel, "A Measurement of the Cross-Section for Detachment of Electrons from H^- by Electron Impact," Proc. Roy. Soc. **A299**, 525 (1967).

5. G. Tisone and L. M. Branscomb, "Detachment of Electrons from H^- by Electron Impact," Phys. Rev. Lett. **17**, 236 (1966).

6. H. A. Thiessen, Los Alamos Scientific Laboratory internal memorandum, October 12, 1970.

7. K. A. Brueckner, "Notes on Stripping of H^- by Hydrogen," Physical Dynamics, Inc. (unpublished) (1975).

8. *Methods of Experimental Physics*, Vol. 7, Part A, 184 (1968) B. Bederson and W. Fite, Eds.

9. A. J. Lieber, R. F. Bentley, J. A. Farrell, T. D. Hayward, J. C. Hopkins, G. P. Lawrence, D. J. Liska, and J. E. Spencer, "WNR Storage Ring Stripper Experiment," (unpublished proposal) (1972).

10. T. D. Hayward, E. A. Knapp, G. P. Lawrence, and R. F. Bentley, "Measurement of the Emittance Growth in H^- Stripping," (unpublished proposal) (1974).

11. D. Bohm, E. H. S. Burhop, and H. S. W. Massey, in *The Characteristics of Electrical Discharges in Magnetic Fields*, A. Guthrie and R. K. Wakerling, Eds. (McGraw-Hill, NY, 1949).

12. F. F. Chen, in *Plasma Diagnostics Techniques*, R. H. Huddlestone and S. L. Leonard, Eds. (Academic Press, NY, 1965).

13. A. von Engel, *Ionized Gases* (Oxford at the Clarendon Press, 1955), pp. 51-56.

14. P. W. Allison, E. A. Meyer, D. W. Mueller, and R. R. Stevens, Jr., *Performance of the LAMPF H^- Injector*, Proc 2nd Symp. Ion Sources and Formation of Ion Beams, Berkeley, California, Oct. 1974, Lawrence Berkeley Laboratory report LBL-3399, VIII-4.

15. J. E. Osher, F. J. Gordon, and G. W. Hamilton, *Production of Intense Negative Ion Beams*, Proc. 2nd Intern. Conf. Ion Sources, Vienna, Sept. 1972, F. Viehböck, H. Winter, and M. Bruck, Eds. (II. Institute für Experimentalphysik der Technischen Hochschule Wien), p. 876.

16. G. I. Dimov and G. V. Roslyakov, *Formation of Negative Hydrogen and Helium Beams by Charge Exchange in Sodium Vapor*, Report IYAF-75-73, Institute of Nuclear Physics, Siberian Section, USSR Academy of Sciences, Novosibirsk, USSR, 1973 (Brookhaven National Laboratory translation).

17. Y. I. Belchenko, G. I. Dimov, and V. G. Dudnikov, *Surface-Plasma Source of Negative Ions*, Proc. 2nd Symp. Ion Sources and Formation of Ion Beams, Berkeley, California, Oct. 1974, Lawrence Berkeley Laboratory report LBL-3399, VIII-1.

18. V. G. Dudnikov, *Surface-Plasma Source of Negative Ions with Penning Geometry*, Institute of Nuclear Physics, Siberian Section, USSR Academy of Sciences, Novosibirsk, USSR, 1975. (Los Alamos Scientific Laboratory translation, LA-TR-75-4).

19. M. E. Kishinevsky, *On the Mechanism of Secondary Ion Emission*, Preprint IYAF-116-73, Institute of Nuclear Physics, Siberian Section, USSR Academy of Sciences, Novosibirsk, USSR, 1973. (Los Alamos Scientific Laboratory translation LA-TR-75-4).

20. J. R. Hiskes, *Hypothesis for the Mechanism of Negative Ion Production in the Surface-Plasma Negative Hydrogen Ion Source*, Lawrence Livermore Laboratory report UCID-16765, March 26, 1975.

21. G. I. Dimov and G. V. Roslyakov, *An Investigation of a Pulsed Charge-Exchange Source of Negative Hydrogen Ions*, Preprint IIF-35-73, Institute of Nuclear Physics, Siberian Section, USSR Academy of Sciences, Novosibirsk, USSR, 1973. (Los Alamos Scientific Laboratory translation LA-TR-73-47).

22. A. J. Lieber, *Weapons Nuclear Research Facility (WNRF) Storage Ring—Technical Study*, Los Alamos Scientific Laboratory report LA-5372 (1973).

23. J. E. Osher and G. W. Hamilton, *An Intense 1 keV Ion Source for Controlled Fusion Research*, Proc. 1st Symp. Ion Sources and Formation of Ion Beams, Upton, New York, Oct. 1971, Brookhaven National Laboratory report BNL-50310, p. 157.

24. K. H. Berkner, W. R. Baker, W. S. Cooper, K. W. Ehlers, W. B. Kunkel, R. V. Pyle, and J. W. Steams, *Performance of LBL 20-keV, 10-A and 50-A Neutral-Beam Injectors*, Proc. 2nd Symp. Ion Sources and Formation of Ion Beams, Berkeley, California, Oct. 1974, Lawrence Berkeley Laboratory report LBL-3399, VI-12.

25. W. Grüebler, P. A. Schmelzbach, V. König, and P. Marmier, *Charge Exchange Collisions Between Hydrogen Ions and Alkali Vapor in the Energy Range of 1 to 20 keV*, Helv. Phys. Acta. 43, 254 (1969).

26. Y. M. Khirnyi and L. N. Kochemasova, *Charge Exchange of Protons Into Negative Ions on Cesium*, Prib. i Tekh. Eksper. 3, 56 (1970).

27. M. Bacal and W. Reichelt, *Metal Vapor Confinement in Vacuum*, Rev. Sci. Instr. 45, 769 (1974).

28. V. P. Golubev, G. A. Nalivaiko, and S. G. Tsepakin, *The Source of Negative Ions*, Proc. 1972 Proton Linear Accelerator Conf., Los Alamos, New Mexico, October 10-13, 1972, Los Alamos Scientific Laboratory report, LA-5115, p. 356.